GFZ

Helmholtz-Zentrum POTSDAM

Sinkholes, subsidence and subrosion on the eastern shore of the Dead Sea as revealed by a close-range photogrammetric survey

Djamil Al-Halbouni[a,], Eoghan P. Holohan[a,d], Leila Saberi[a], Hussam Alrshdan[b], Ali Sawarieh[b], Damien Closson[c], Thomas R. Walter[a], Torsten Dahm[a]

[a]*GFZ German Research Centre for Geosciences, Section 2.1, Telegrafenberg, Potsdam 14473, Germany.*
[b]*Ministry of Energy and Mineral Resources, Mahmoud Al Moussa Abaidat Street, Amman 140027, Jordan.*
[c]*Eurosense Belfotop, Remote Sensing Applications Department, Nerviërslaan 54, B-1780 Wemmel, Belgium.*
[d]*Now at: UCD School of Earth Sciences, University College Dublin, Belfield, Dublin 4, Ireland.*

Abstract

Ground subsidence and sinkhole collapse are phenomena affecting regions of karst geology worldwide. The rapid development of such phenomena around the Dead Sea in the last four decades poses a major geological hazard to the local population, agriculture and industry. Nonetheless many aspects of this hazard are still incompletely described and understood, especially on the eastern Dead Sea shore. In this work, we present a first low altitude ($< 150\,\mathrm{m}$ above ground) aerial photogrammetric survey with a Helikite Balloon at the sinkhole area of Ghor Al-Haditha, Jordan. We provide a detailed qualitative and quantitative analysis of a new, high resolution digital surface model ($5\,\mathrm{cm}\,\mathrm{px}^{-1}$) and orthophoto of this area ($2.1\,\mathrm{km}^2$). We also outline the factors affecting the quality and accuracy of this approach.

Our analysis reveals a kilometer-scale sinuous depression bound partly by flexure and partly by non-tectonic faults. The estimated minimum volume loss of this subsided zone is $1.83 \cdot 10^6\,\mathrm{m}^3$ with an average subsidence rate of $0.21\,\mathrm{m}\,\mathrm{yr}^{-1}$ over the last 25 years. Sinkholes in the surveyed area are localized mainly within this depression. The sinkholes are commonly elliptically shaped (mean eccentricity 1.31) and clustered (nearest neighbor ratio 0.69). Their morphologies and orientations depend on the type of sediment they form in: in mud, sinkholes have a low depth to diameter ratio (0.14) and a long-axis azimuth of NNE–NE. In alluvium, sinkholes have a higher ratio (0.4) and are orientated NNW–N. From field work, we identify actively evolving artesian springs and channelized, sediment-laden groundwater flows that appear locally in the main depression. Consequently, subrosion, i.e. subsurface mechanical erosion, is identified as a key physical process, in addition to dissolution, behind the subsidence and sinkhole hazard. Furthermore, satellite image analysis links the development of the sinuous depression and sinkhole formation at Ghor Al-Haditha to preferential groundwater flow paths along ancient and current wadi riverbeds.

Keywords: Photogrammetry, Sinkholes, Subsidence, Subrosion, Karst, Dead Sea, Ghor Al-Haditha

1. Introduction

Ground subsidence phenomena occur all over the world due to both natural and anthropogenic causes (cf. e.g. Kohl, 2001; Denizman, 2003; Caramanna et al., 2008; Closson et al., 2009; Parise and Lollino, 2011; Dahm et al., 2011; Dreybrodt, 2012; Gutierréz et al., 2014; Kotyrba, 2015; Parise, 2015). Sinkholes in particular are enclosed depressions of the soil/rock surface caused by subsurface chemical dissolution (Waltham et al., 2005) or subsurface mechanical erosion (Parise, 2010), termed subrosion in the following as in e.g. Dahm et al. (2011). They typically span a submeter to hundreds of meters scale, both for depth and diameter (cf. e.g. Goldscheider and Drew, 2007; Filin et al., 2011; Gutierréz et al., 2014; Messerklinger, 2014). Sinkholes are genetically classified into two main groups: solution and subsidence sinkholes (Waltham and Fookes, 2005; Gutiérrez et al., 2008; Beck, 2012). Subsidence sinkhole end-member classification refers to the affected material (cover, caprock or bedrock) and the process of formation (collapse, sagging or suffosion) (cf. Gutierréz et al., 2014). In karst environments, collapse sinkholes are often related to subsurface void collapse (Hatzor et al., 2010; Parise and Lollino, 2011; Dreybrodt, 2012; Gutiérrez et al., 2014; Waltham, 2016), where stress conditions exceed material strength in the surroundings, frequently related to sudden water-level changes (Tharp, 1999, 2002; Shalev and Lyakhovsky, 2012; Lollino et al., 2013) or seismic activity (e.g. L'Aquila earthquake, Kawashima

et al. (2010); Parise et al. (2010)). These phenomena are most hazardous due to the rapid cavity roof breakdown and include not only potential direct losses of life, but also damage to economically important buildings, land (Parise, 2010; Krawczyk and Dahm, 2011) and infrastructure (e.g. Brinkmann et al., 2008; Dahm et al., 2011; Gutierréz et al., 2014). The opposite, a slow subsidence process with long-term sinkhole growth, holds for sagging or suffosion sinkholes and is considered as less hazardous from an engineering point of view (Gutierréz et al., 2014).

The sinkhole formation at the Dead Sea (Fig. 1A) has increased sharply in the last decades (Arkin and Gilat, 2000; Yechieli et al., 2015). This development has been associated with the significant lake-level drop since the 1950s (Taqieddin et al., 2000) from $\approx 393\,\text{m}$ to $430\,\text{m}$ (20.10.2015) below sea level. Anthropogenic influence is considered to be the main reason for this decline, i.e. large water irrigation projects in the northern part along the Jordan river catchment (Gavrieli and Oren, 2004; Bowman et al., 2010), extensive use of Dead Sea brine for Potash production (Lensky et al., 2005; Abelson et al., 2006) as well as the increasing need for drinking and irrigation water due to a growing population (World Bank, 2016) and climatic changes (Menzel et al., 2007; MWI, 2013; Al-Omari et al., 2014; Odeh et al., 2015). Attention to the sinkhole phenomenon has increased, since touristic regions, highways, agricultural land as well as industries (e.g. Ein Gedi, Ghor Al-Haditha, Arab Potash factory) have become seriously affected (Nof et al., 2013; Closson et al., 2013; Closson and Abou Karaki, 2015).

Email address: halbouni@gfz-potsdam.de (Djamil Al-Halbouni)

An important scientific question concerns the mechanical and chemical processes of sinkholes formation: is the formation mechanism controlled by pure salt-dissolution (Frumkin et al., 2011; Oz et al., 2016), faults (Closson and Abou Karaki, 2009), both (Ezersky and Frumkin, 2013; Closson and Abou Karaki, 2013; Ezersky et al., 2014) or subrosion (Arkin and Gilat, 2000)? Hereby the role of rock properties and detailed material/(sub)surface water movement is essential for understanding sinkhole evolution and development of early-warning scenarios (Waltham et al., 2005; Parise, 2008; Lollino et al., 2013; Gutierréz et al., 2014).

In this context, we conducted a high resolution close-range photogrammetric (Burner et al., 1983; Luhmann et al., 2014) investigation of the active sinkhole area of Ghor Al-Haditha in Jordan (cf. DESERVE project in Kottmeier et al., 2016) in Oct. 2014 and 2015 (Fig. 1B,C). We used a cost-efficient and robust helium balloon technique for areas, such as this one, where legal permissions for other UAV based surveys and access to satellite images are difficult to attain.

Photogrammetry has been applied extensively on the western shore of the Dead Sea, e.g. for mapping stream channel incision (Bowman et al., 2010), ground-water flow paths (Mallast et al., 2011) and is currently used for spring discharge detection (Siebert et al., 2014a). However, rather cost-intensive LiDAR (Laser Imaging, Detection and Ranging) or low resolution satellite based In-SAR (Interferometric Synthetic Aperture Radar) studies have been used for detailed sinkhole characterization (Filin et al., 2011; Nof et al., 2013; Atzori
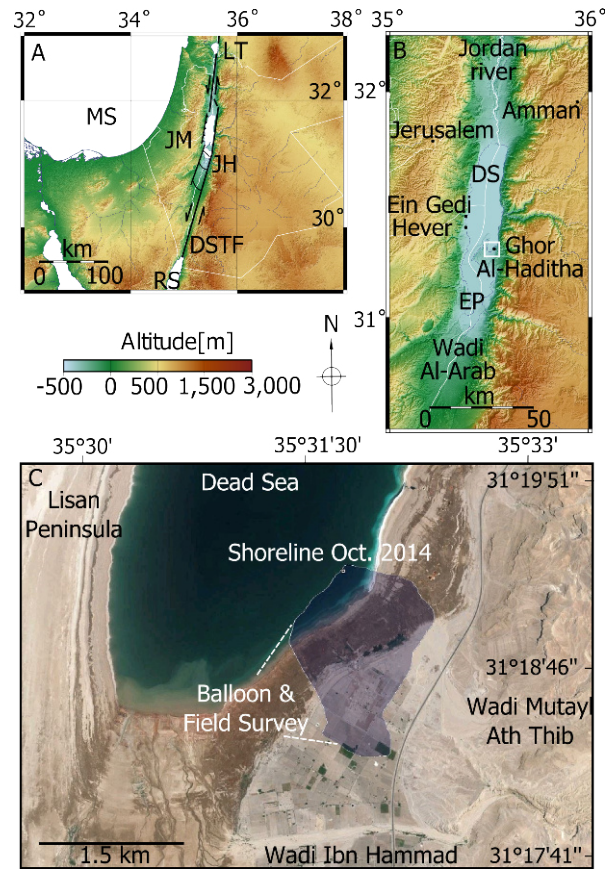
Fig. 1: Location of the Dead Sea and investigation area Ghor Al-Haditha: **A**: Schematic tectonic background of Dead Sea transform fault (DSTF) based on (Bender, 1968; Closson, 2004; Le Béon et al., 2012). MS: Mediterranean Sea, RS: Red Sea, JM: Judean Mountains, JH: Jordanian Highlands, LT: Lake Tiberias. Topographic data are based on SRTM3 databases (Farr et al., 2007). **B**: Dead Sea and surroundings. The survey area Ghor Al-Haditha in Jordan is located at the SE margin of the Dead Sea basin. DS: Dead Sea, EP: Evaporation Ponds. **C**: Detailed outline of the investigation area and the main wadis. A third river, Wadi Al Madbaa, discharges into the delta system in the southern bay and is located further south outside the shown area. Image is a publically available 2009 Digital Globe image from Google Earth.

3

et al., 2015). Especially on the eastern side of the lake remote sensing studies are still under way (e.g. Al-Ruzouq et al., 2011; Tessari and Floris, 2014, unpublished reports). This is the first study to present a high resolution ($5\,\mathrm{cm\,px^{-1}}$) digital surface model (DSM) and orthophoto of the sinkholes in Jordan.

We firstly introduce the area (Section 2) and then detail the methods used (Section 3). In the result section 4) we demonstrate that at Ghor Al-Haditha a large-scale depression has developed in a zone of former surface water channels. In this main depression, at the boundary between two geological units, the alluvium and mud-flat, sediment-laden artesian springs and stream channels appear, continuing both on the surface and below. Furthermore, we provide an estimation of the minimum volume loss in this area and quantitative evidence for material control on sinkhole morphologies. Limitations of the method, implications and a detailed discussion on structural, lithological and groundwater control of subsidence and sinkhole formation are given in Section 5. Finally, we provide a conceptual model for subsidence and sinkhole formation at Ghor Al-Haditha. This study is hence important for the understanding of sinkhole formation processes both at the Dead Sea and in similar hydrogeological environments and may serve as a basis for future sinkhole hazard and risk assessment.

2. Ghor Al-Haditha sinkhole area

The investigation area is located at the SE shore of the northern Dead Sea basin (Fig. 1B,C), an orthorhombic pull-apart basin of 80 km length, between 5–17 km width and up to 10 km depth of the sediment infill (Ten Brink and Ben-Avraham, 1989; Garfunkel and Ben-Avraham, 1996; Smit et al., 2008). It forms part of the left-lateral Dead Sea Transform Fault System (DSTF, see Fig. 1A), running from the Red Sea to the East Anatolian Fault between the African and Arabian plates (Bender, 1968), with typically a N10–30 ° orientation of the main faults (cf. e.g. Yechieli et al., 2015). In this semi-arid to arid region, the Dead Sea is considered as a hyper-saline terminal lake of the Jordan river (Siebert et al., 2014b); the course of which follows the DSTF.

Marine and lacustrine sediment sequences cover the Dead Sea floor and surroundings (cf. e.g. Bender, 1968; Begin et al., 1974; Garfunkel and Ben-Avraham, 1996; Taqieddin et al., 2000; Frumkin et al., 2011). The most prominent is the late Miocene Usdom (Sedom) formation (2–4 km) of diapiric evaporites found by oil drillings beneath the Lisan Peninsula (Bentor, 1961). On top are the middle-late Pleistocene lacustrine-fluviatile Amora and Samra formations, up to 3 km thick. Exposed at the surface are lacustrine sediments of the late Pleistocene Lisan formation (10–40 m) and recent sediments with thickness of several tens of meters. Kilometer long flats of those lacustrine sediments are nowadays exposed by the Dead Sea regression on both sides of the lake.

The Ghor Al-Haditha sinkhole area lies partly on a piedmont of alluvial fan deposits of Pleistocene to recent age (Taqieddin et al., 2000). It is around 3 km wide and lies between three periodically active wadi systems, Wadi Ibn Hammad, Wadi Mutayl Ath Thib and Wadi Al-Madbaa in the South (Fig. 1C). In 1970, these wadis fed fertile alluvial

4

fan-deltas that were largely used for agriculture; no sinkholes had formed at that time (Fig. 2).

The first sinkholes appeared at Ghor Al-Haditha, south of Wadi Ibn Hamad, in the 1980s, but were quickly filled in. At the beginning of the 1990s, more sinkholes opened north of the Wadi Ibn Hamad river. Following this development, local geological and geophysical studies were initiated to assess the sinkhole hazard (El-Isa et al., 1995). The 'Numeira mixed salts and mud company' started a factory in this area in 1997, but since sinkhole clusters were approaching the factory, more scientific research was undertaken (Taqieddin et al., 2000; Sawarieh et al., 2000; Diabat, 2005; Al-Zoubi et al., 2007; Frumkin et al., 2011; Alrshdan, 2012; Ezersky et al., 2013, partly unpublished reports).

Already in the late 1990s, the main recommendation for both the land farmers and factory was to leave the area, as it was, and is, considered a hazardous zone. In the early 2000s, the most hazardous zone shifted closer to the factory (Kottmeier et al., 2016). The agricultural area was partly abandoned and the factory had to be closed in 2009 (Fig. 3) (Closson et al., 2009, and personal communication by Eng. Emad Talafeha). Sinkholes still develop nowadays (cf. Fig. 3) in the alluvial fans as well as in the more and more exposed former lake bed.

Nontheless, sinkhole occurrence, morphology and development in Ghor Al-Haditha are incompletely understood and remain a topic of high relevance also for the local authorities. We therefore undertook a high resolution photogrammetric survey to provide a more detailed documentation of the sinkholes in the area surrounding the former factory site and to gain new insight into the factors controlling
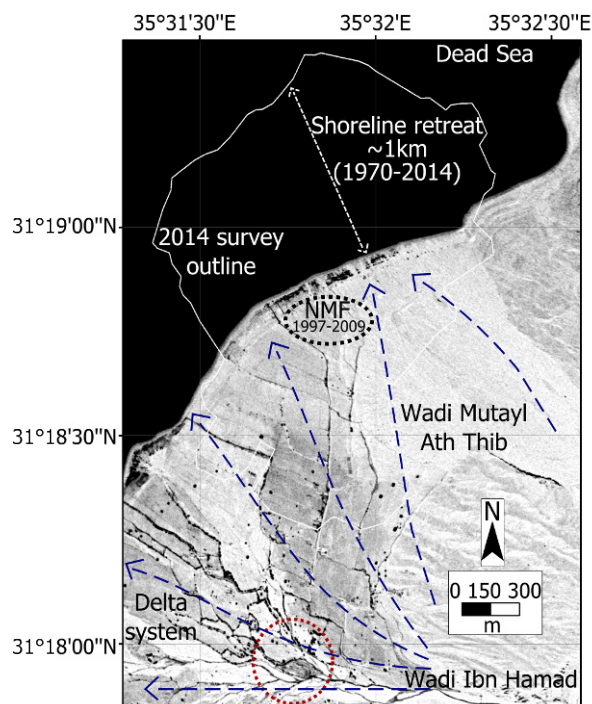
Fig. 2: Corona satellite image of Ghor Al-Haditha from 1970, with overlay of the survey outline. At that time the fan-deltas were strongly used by agriculture and no sinkholes were recorded yet. Since then, the Dead Sea has receded by around 1 km. The first sinkholes appeared in the 1980s near the Wadi Ibn Hamad (red circle), but then approached the Numeira Mud factory (NMF). Blue arrows show schematically the groundwater flow pattern in this area in the year 1999 based on water level measurements in wells and springs mentioned in the unpublished report of Sawarieh et al. (2000). The general trend was towards N–NW from the alluvial fans towards the Dead Sea (black coloured), with an estimated hydraulic gradient of $> 30\,\mathrm{m\,km^{-1}}$.

their formation (cf. Section 5).

3. Data acquisition and processing

3.1. Close-range photogrammetry

Aerial images of the area were acquired by a Ricoh GRII camera with 16.2 MP resolution, an angle of view of 28 mm and a focus length of 13.7 mm. It was mounted on a kite-stabilised, helium-filled balloon (Helikite) of $4.5\,m^3$ size that flew at between 100 and 150 m altitude (Appendix Fig. A.1A). For the requirements of the acquired near-field image pairs (see algorithm description below), the balloon offered the best possibilities (cf. also Walter (2014)), as in windy areas like at the Dead Sea the kite stabilizes the azimuth and incidence angle. The photo footprint at 100 m flight height was about 125 x 180 m, leading to $\approx 3.6\,cm\,px^{-1}$ ground resolution for an image at nadir. The calculated mean ground resolution for all processed images was $6.7\,cm\,px^{-1}$. For geo-referencing, over 60 ground control points (GCPs) were measured by a Differential Global Positioning System (DGPS) with up to 10 cm horizontal and vertical accuracy (Appendix Fig. A.1B), using a real-time global satellite-based augmentation system (Trimble Omnistar XP.).

The aerial images of Oct. 2014 were used to build a 3D digital surface model and orthophoto. A Multiview Stereopsis technique (Furukawa and Ponce, 2010) of the structure-from-motion close-range photogrammetric method (Harwin and Lucieer, 2012; Luhmann et al., 2014) was applied, as implemented in the commercial software package PhotoScan Pro (Agisoft LLC). We followed mainly the processing
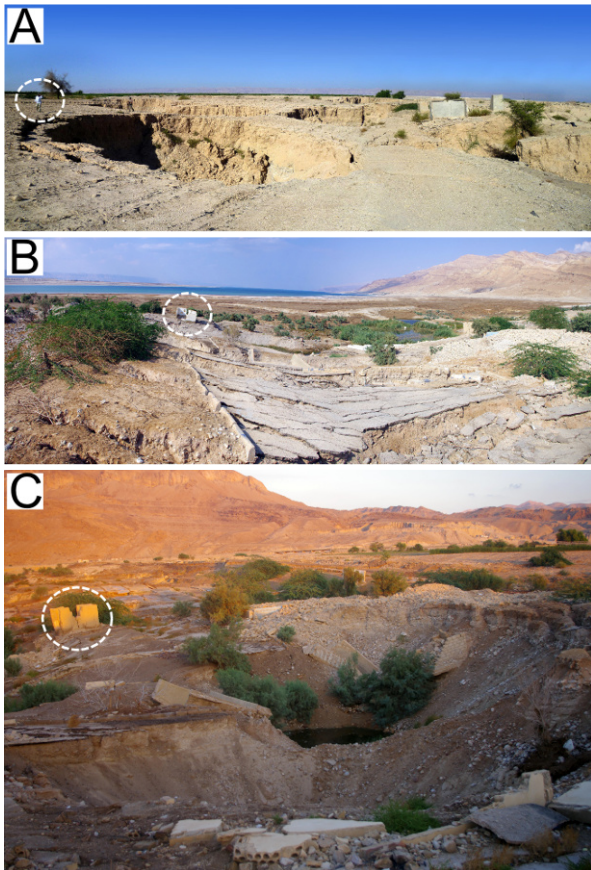

Fig. 3: Damage of infrastructure at Ghor Al-Haditha sinkhole site. **A**, **B**: Panorama views of deep cover-collapse sinkholes that destroyed agricultural buildings and roads. **C**: Sinkholes and subsidence destroyed the 'Numeira mixed salts and mud company' at the alluvium/mud-flat contact. Dashed circles mark scales (persons, buildings).

scheme shown in Fig. 4 and described in detail in e.g. Agisoft (2013) and Leon et al. (2015).

Photogrammetry in general uses single or multi-image photographic recordings for the 3D reconstruction and interpretation of objects or areas of interest (Luhmann et al., 2014). The interior 2D image coordinate system (x', y') of each point (P), defined by the camera of the acquired photograph, is transformed by mathematical models into the exterior 3D object space (X, Y, Z) (Förstner and Wrobel, 2013), see bundle adjustment technique in Appendix A.1. For this purpose a record of a single image point needs to be available in at least two photographs, providing intersecting image rays. For a high accuracy in all coordinates, at least three to four photos are desirable (Luhmann et al., 2014). Therefore common aerial photo surveys with photogrammetric purpose tend to have 50–70 % overlap between each acquired image pair and recordings at different incidence angles.

Each point of the generated sparse point cloud is identified by its particular information about geometric position and radiometric data (Luhmann et al., 2014), like grey value, RGB, gradients and intensity. This requires ideally similar image acquisition conditions (light sources, shadow distribution and camera sensor), which in the field can be fulfilled by repeated measuring at the same time of the day or selection of appropriate time spans. In our case the light conditions are of special importance for the edge detection algorithm of structures in the field, therefore photos were taken mainly from late morning to early afternoon.

By using relative positions of the detected sets of overlapping image points, a multi-image trian-
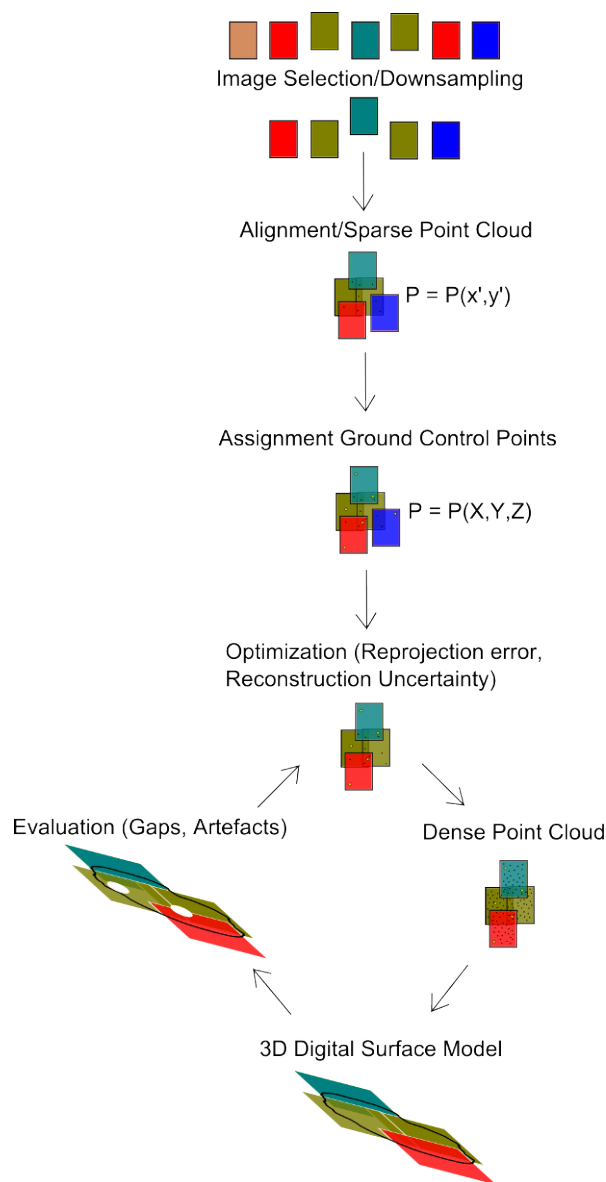
Fig. 4: Applied processing scheme of the structure-from-motion close-range photogrammetric method. See text for a detailed description.

gulation and space resection (see Appendix A.1) is performed taking into account the camera calibration. In PhotoscanPro the camera position is determined after primary sparse point cloud image triangulation, by using information like camera type, focal length and resolution from the metadata of the images to determine distortions. When survey information on the object surface (geometries and reference points) exists, the normal equations are over determined and the bundle is transferred into a local or global (geo-referenced) coordinate system, building the Dense Point Cloud (Fig. 4). The final adjusted bundle contains 3D information of the measured object or area with a quality (coordinate residuals) mainly determined by the accuracy of the reference measurements, the correlation of physical parameters of the pixel comparison algorithm and systematic errors. An evaluation loop is applied and erroneous regions have been improved by carefully adding further images, manual point cloud editing, non-linear deformation removal (Agisoft, 2013) and model cropping and merging, so that the final optimized DSM is achieved.

To place the photogrammetric results into the geomorphological context, we also analysed a set of satellite images with $1.8\,\mathrm{m\,px^{-1}}$ resolution, acquired by the Corona (USGS, 2015) mission KH-4B 1111 from 1970-08-05. This represents the time when the shoreline was still stable, corresponding to the superficial limit between alluvium and mud-flat in our area (cf. Section 2). Additionally, we analyzed satellite images from Quickbird-2 ($0.6\,\mathrm{m\,px^{-1}}$) and Worldview-2 ($0.46\,\mathrm{m\,px^{-1}}$) from 2012. For further analysis of the DSM, GIS has been used. It enabled a detailed mapping of struc-tures and morphological features in the survey area. Details of the algorithms used can be found in Esri (2015) and De Smith et al. (2015). GIS and aerial photo analysis was complemented by field observations made in 2014 and 2015.

3.2. Accuracy and limitations

As a first step, a sensitivity study on the northern half of the surveyed area has been performed to investigate the role of reference marker selection. In general, at least three GCPs should exist in a survey area, while a higher accuracy and a more even distribution of GCPs increase the accuracy of the derived DSM (Harwin and Lucieer, 2012; Luhmann et al., 2014). Different GCP distributions have been tested and an elevation difference (reprojection error) of the individual Test-DSM with respect to the measured GCP values has been calculated (Figs. 5 and 6). The term elevation is used here and in the following with reference to the geoid equipotential surface of the Earth.

Gaps and artefacts (cf. Fig. 8) generally occur due to downsampled image sets, significantly different light conditions in the overlapping regions, vegetation, or at the margins of the area. A crucial factor for the existence of gaps in the DSM is the number of image overlaps (Fig. 5A). Even large numbers of GCPs, which means a strong interpolation of elevation data, cannot counterbalance a low number of image tie points. A GCP selection orientated roughly perpendicular (NE–SW) to the overall topographic gradient shows the highest root mean square error ($\bar{R}$) values (Fig. 5B and 6B), while the same line simply orientated parallel (NW–SE) and hence spanning a large elevation
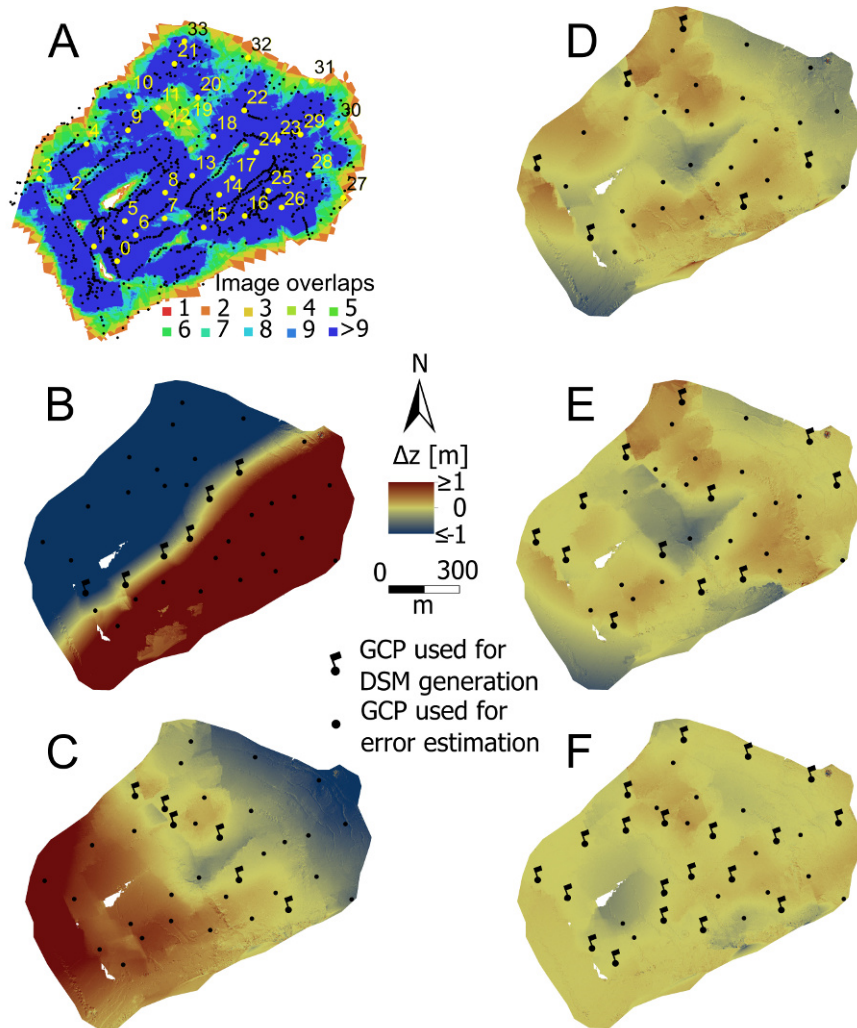
Fig. 5: DSM quality analysis for the northern half of the survey area. **A**: Agisoft image overlaps. Missing images lead to a lack of tie points, as seen nicely at the upper central part and the gap (white) areas. This hence will hinder the optimal referencing of the image pairs. Black circles refer to camera locations. Numbers indicate IDs of control points (yellow circles) used for error estimation. **B-F**: Elevation differences with reference to a DSM generated with all 33 ground control points, the lowest error DSM for this part (cf. Fig. 6B). Here, black circles indicate GCPs used for error estimation while circles with flags mark the control points used for georeferencing the individual DSM. **B**: Six NE–SW aligned GCPs. $|\Delta z|$ is higher than 1 m as the GCPs tend to follow a topographic contour line. **C**: Six NW–SE aligned GCPs. $|\Delta z|$ is lower than at **B**, because of the perpendicularity to topographic contour lines. **D**: Six GCPs approximately aligned as a rectangle. This distribution strongly improves the mismatch. **E**: Twelve well distributed GCPs. The overall mismatch is slightly lower while locally areas with high mismatch remain. **F**: Twenty well distributed GCPs.
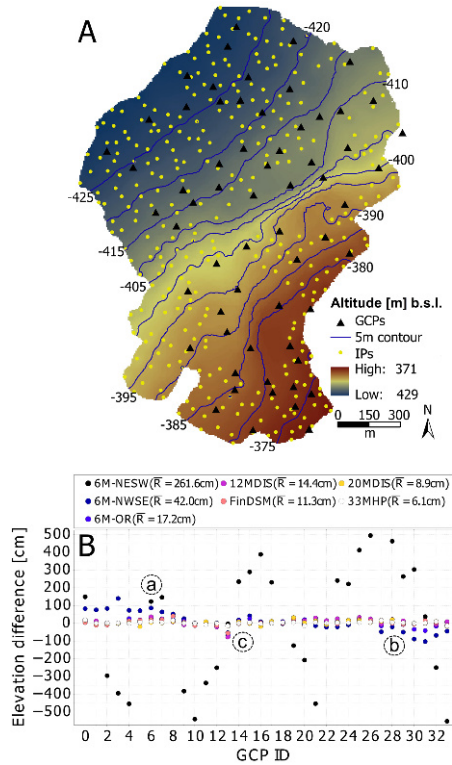
Fig. 6: Georeferencing and error analysis of the DSM. **A**: Position of all ground control points used for georeferencing the final DSM (black triangles). Note that the distribution is plotted before final optimization of the DSM, resulting in some GCPs outside the cutted margins. The background topography is an interpolated pre-subsidence DSM used for volume loss estimation of the Ghor Al-Haditha sinkhole area. The main depression and canyons have been omitted in the placement of the fixed boundary points (IP, yellowish circles). **B**: Reprojection error analysis for the northern half of the survey area. A comparison of the calculated DSMs of varying GCP selection with original in-field measured elevations is shown (cf. Fig. 5 and part A for GCP locations). Markers **a** and **b** emphasize the spatial distribution effect, where the DSM of six NE–SW aligned GCPs performs badly at the margins and well at the center (GCP ids 12-20). The behaviour of GCP id 13 at marker **c** highlights that even high numbers of image projections do not avoid errors in elevation estimation, if certain GCPs are not included.

gradient, performs much better (Figs. 5C and 6B). The lowest mismatch is achieved by using all GCPs in this area (33MHP), while the selection of 20, 12 or even only six well-distributed GCPs (20MDIS, 12MDIS and 6M-OR) still yields a very good result and shows similar mismatches (Figs. 5D-F and 6B). The most important criteria hence for DSM accuracy are the equal spatial distribution of the marker points and the accuracy of the GCP positions.

4. Results

We present a high resolution orthophoto and digital surface model of the surveyed sinkhole area of Ghor Al-Haditha. This is followed by a detailed qualitative and quantitative analysis of structural and morphological aspects of the subsidence phenomena. Combining the photogrammetry with satellite image analysis we then describe evidence for surface and subsurface water flow and its relationship to the morphological and structural phenomena at Ghor Al-Haditha.

4.1. Orthophoto and digital surface model

From close-range photogrammetry, we generated a high resolution orthophoto (Fig. 7) and digital surface model (DSM, Fig. 8). Marked in both images for reference are the most important morphological features and the locations of aerial and ground-based photos. The total size of the surveyed area is ca. $2.1\,\mathrm{km}^2$.

After the GCP selection procedure, a preliminary DSM, based on more than 3100 photos, was generated stepwise in three overlapping model areas due to computation limitations. Following corrections with the evaluation loop technique described

above (Section 3), the final DSM is based on approximately 8400 photos. A modeling mesh of $6.56 \cdot 10^6$ vertices was used to produce a high resolution ($6.7\,\mathrm{cm\,px^{-1}}$) orthophoto (Fig. 7) and final 3D DSM (Fig. 8) of the area of interest. The reprojection error of the final DSM is higher than the optimal value calculated for the northern part (Fig. 6B). This is due to lower DGPS accuracy, more image-pairs and markers missing at the margins (cf. final GCP distribution in Fig. 6A). Nonetheless the final accuracy of the DSM is around $10/11/15.2\,\mathrm{cm}$ (x,y,z). The effective DSM resolution is $29.6\,\mathrm{cm\,px^{-1}}$ with a point density of $11.31\,\mathrm{pt\,m^{-2}}$, while interpolation for smoother subsequent analysis leads to a feasible higher resolution of $5\,\mathrm{cm\,px^{-1}}$.

In the orthophoto and DSM (Figs. 7 and 8) we distinguish the two principally affected surface materials: (1) the Dead Sea mud and salt sequences of the former Dead Sea lake bed (cf. Appendix Fig. A.2C) and (2) the alluvial fan sediments of the Lisan formation (cf. Section 2). The mud appears dark reddish-brownish in the northern part of the area with individual whitish areas of exposed evaporites. A sharp boundary delimits the mud from the bright greyish alluvial sediments in the southern part.

The distinction between both main geological units is also very clearly visible in the DSM. The topographically high area (reddish) corresponds to the alluvial fans, while the low lying area (blueish) corresponds to the mud-flat. The observable and marked transition zone shows a relatively sharp drop in elevation between approximately -393 and $-407\,\mathrm{m}$. This corresponds to the old, long-term stable and vegetated shoreline of the Dead Sea.

## 4.2. A several hundred metre scale sinkhole-hosting depression

The DSM reveals a distinctive bright area marking a subtle, large-scale, sinuousoidal depression. The limits of this depression have been determined visually rather than by GIS tools following suggestions from Doctor and Young (2013). Meter-scale concentric faults and ground cracks bound the area and are visible in the orthophoto; a ground based view is given in Appendix A.2 (Fig. A.2A). The gentle main depression area covers roughly $0.34\,\mathrm{km^2}$ and contains approximately $85\,\%$ of the identified sinkholes. The deepest point in the main depression lies at $-424\,\mathrm{m}$ elevation, exactly at the spring point of an active stream that is described more in detail in Section 4.5.

4.3. Sinkhole distribution and clustering

The total number of sinkholes identified in the surveyed area is 298; in alluvium 193 and in mud 105. Closeup DSMs of representative sinkholes in these materials are shown in Fig. 8A,B. Twenty-four of those counted as in mud are at the vegetated transition between both surface material types. Eleven sinkholes are filled with water, most of them in the mud. The total area affected by sinkholes, including the northward possible continuation of the depression and marginal sinkholes, is approximately $0.45\,\mathrm{km^2}$, leading to a density estimation of $6.6\,\mathrm{sinkholes\,ha^{-1}}$.

Most of the sinkholes in the surveyed area are clustered into a roughly NNW–SSE orientated zone on the alluvium and ENE–WSW orientated zone on
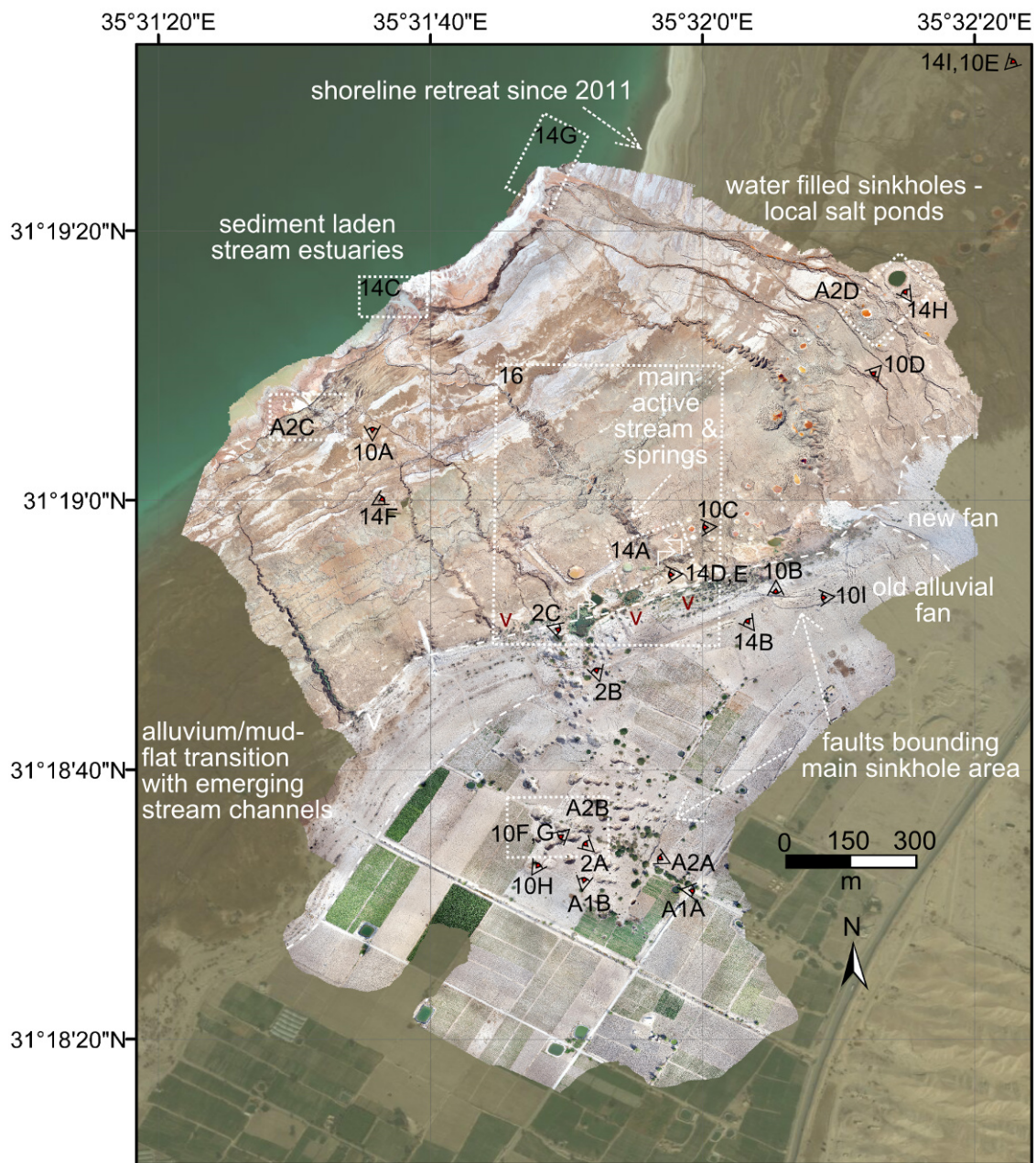
Fig. 7: High resolution ($6.7\,\text{cm}\,\text{px}^{-1}$) orthophoto of Ghor Al-Haditha sinkhole area. The orthophoto lies upon a satellite image background from February 2011 provided by ArcGIS basemap source Digital Globe with $15\,\text{m}\,\text{px}^{-1}$ resolution. Indicated are the most important large-scale morphological features as well as locations of field observation and aerial photos. This dynamically changing area contains very recently formed channels (center, N) and alluvial fans (center, E). Concentric normal faults partly bound the main sinkhole area. Streams and springs carry sediments into the lake. Sinkhole-related pools and salt ponds are observable in the mud-flat. Vegetation (v) and stream channels appear at the alluvium/mud-flat boundary.

12
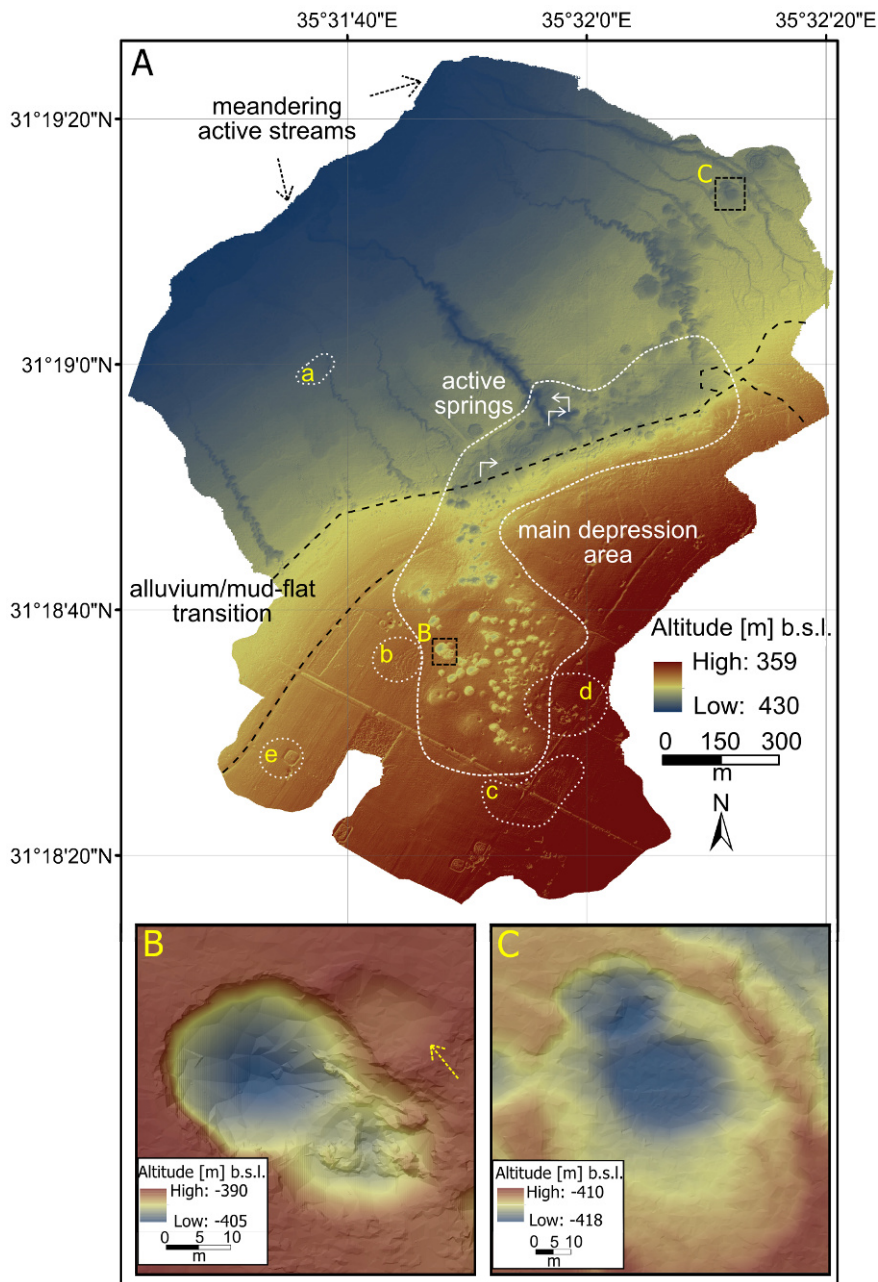
Fig. 8: High resolution ($5\,\mathrm{cm\,px}^{-1}$) digital surface model of Ghor Al-Haditha sinkhole area. **A**: Shaded relief image of topography within the surveyed part of the Ghor Al-Haditha sinkhole area resulting from the DSM. The main depression area, the alluvium/mud-flat boundary and the active groundwater springs are indicated. A further continuation of the main depression area to the NE can be inferred from the DSM. **B**: Closeup of a representative sinkhole in the alluvium. **C**: Closeup of a representative sinkhole in the mud. Dotted lines mark either data gaps (**a**), uncertain areas with higher error (**b**) and identified artefact zones (**c**), resulting from different light conditions or missing images. Trees may rarely be confounded with or hide sinkholes (**d** and closeup **B**) and artificial water ponds are recognizable due to their elevated rims (**e**, see also truncated irrigation pond marked with an arrow in **B**).

13

Table 1: Nearest neighbor comparison of sinkholes for Ghor Al-Haditha sinkhole area. NNR is the nearest neighbor ratio, P the significance level and $\bar{d}$ the mean distance between sinkholes. As all $NNR < 1$, the distribution is significantly clustered.

|	alluvium	mud	total
NNR	0.64	0.83	0.69
P-value	< 0.01	< 0.01	< 0.01
$\bar{d}$[m]	16.18	24.03	18.66

the mud sediments straddling the alluvium/mud-flat boundary.

The observed clustering is quantified via a GIS nearest neighbor comparison (Esri, 2015). A random distribution yields a nearest neighbor ratio $(NNR) = 1$. $NNR < 1$ means a clustered distribution, while $NNR >> 1$ means a dispersed distribution. With $NNR < 1$ the distribution for both mud- and alluvium-hosted sinkholes is significantly clustered with a mean intra-cluster distance of 18.7 m between two sinkholes (Table 1). According to the relative density map (Fig. 9), the majority of those clusters is inside the main depression.

4.4. Material control on subsidence morphology and structure

4.4.1. Qualitative observations

As identified in the DSM and orthophoto, the area contains two main geological units (Fig. 10A,B), covered by a few meters of topsoil: old to recent poorly consolidated, coarse to fine grained alluvial fan deposits (alluvium) and interbedded, lacustrine, fine grained clay and evaporites (mud-flat). The Dead Sea mud (Fig. 10A) comprises dark organic material (brownish-reddish to olive-
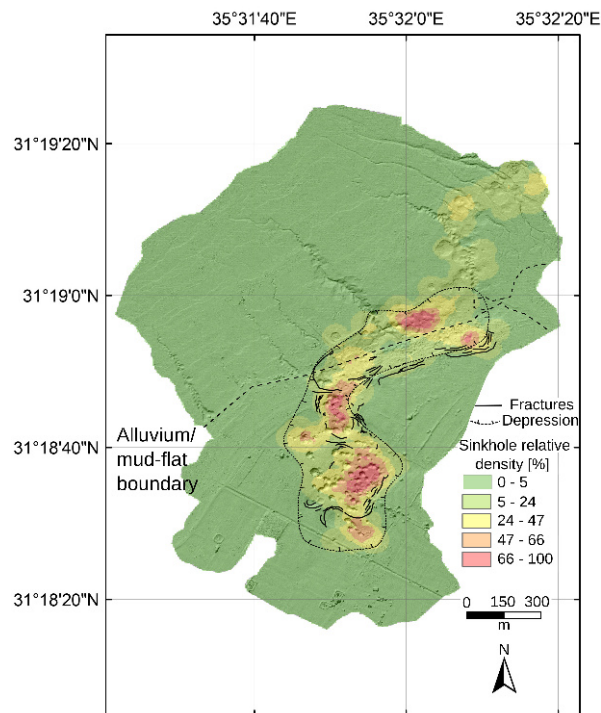
Fig. 9: Relative density distribution of sinkholes. Each sinkhole is represented by a uni-sized point at its center. The density is calculated via the kernel density calculation by GIS, using standard search radius and a smooth quadratic and tapered surface for each point (Esri, 2015). The resulting maximum number of 2496 pixels per unit area has been used for normalization of the colorscale. Clearly, a local clustering with changing bulk cluster orientation is observed (red areas). In alluvium the high density clusters tend to strike NNW–N, and in mud from NE–E. The main fractures bounding the depression area are indicated.

14

greyish), greyish calcite and whitish aragonite laminae (cf. e.g. Khoury, 2002). It is also referred to as 'lime carbonates' (Frydman et al., 2008) because of the high content of carbonate minerals (Khlaifat et al., 2010). It even contains idiomorphic halite (NaCl) crystals, in places up to 50 % by volume. Locally, individual evaporite layers (Fig. 10A and Appendix Fig. A.2C) 1 cm to 1.5 m thick were observed in sections along the stream channels. The alluvial sediments comprise a mixture of clasts of sandstone, limestone, marl, chert and basalt, with grain sizes varying from fine grained sand to pebbles and even boulders (Fig. 10B). The material compound is partly to poorly cemented.

Important morphological differences have been observed between the subsidence phenomena of the mud-flat and alluvial fans, as highlighted in a slope distribution map (Fig. 11) and in Closeup DSMs for representative sinkholes in Fig. 8A,B. In the mud, sinkholes are generally wide but shallow (Figs. 8B and 10C), sometimes coalesced into uvala like structures. Slopes of the margins are more gentle (0 ° to 90 °), similar to the slopes at canyon slumps. Nevertheless, some sinkholes in mud with relatively strong evaporitic cover show overhanging margins (Fig. 10E). Many sinkholes in mud display a wide peripheral zone of extensional fracturing and outward-rotated strata (Fig. 11F). This is structurally and morphologically similar to landslides or slumps found adjacent to the deeper stream channels (Fig. 11G); these slumps are bound by listric normal faults (Fig. 10D). Despite overprinting effects, a distinction between sinkholes and slumps is possible. Slumps are open on the streamward side and generally spatially connected to the outer-arc of the stream meanders (cf. DSM in Fig. 8). Finally, slump boundaries do not cross the associated stream channel, as would be so in the case of a sinkhole intersected by a stream.

In the alluvium, sinkholes generally show steeper internal slopes (between 45 ° and 90 °) and in several places linear alignments or coalescence (Fig. 11C,D). Some of these deep and narrow sinkholes (Figs. 8A and 10F) display inward-tilted (toppled) sidewall blocks (Fig. 10G), or even partially overhanging side walls (Fig. 10H). More rarely, subsidence in the alluvium expresses locally as 'sag' structures with a wide 'halo' of concentric cracks (Fig. 11B). These non-collapsed depression areas may show compression ridges in the center. Within the alluvium numerous cracks, fault scarps of up to 2 m height and crevasses with depths of up to 4 m (Figs. 10I and 11A) adjoin the deeper points of the depression zone (Fig. 9).

4.4.2. Quantitative observations

Quantitative analysis of sinkhole geometries requires an error estimation for sinkhole depth and diameter. It is based on a manual determination of the standard deviation of long, short axis and depth. A randomly chosen sample set of 40 sinkholes has been used for this purpose. Considering the horizontal error of the DSM, the mean relative error for sinkhole diameter estimation is 17.6 % and for the depth 27.9 %. Those sinkholes filled with water and most of those in the transition zone between the cover materials are excluded from further detailed quantitative analysis.

The mode of sinkhole diameter distribution (Fig. 12A) in alluvium is between 4–12 m. In mud

15

Fig. 10: Geology, structures and sinkhole morphologies at Ghor Al-Haditha. **A**: Mud-flat deposits, comprising laminated silt and clay, locally interbedded with evaporite layers up to 1.5 m thick (**a**) and ideomorphic halite crystals (**b**). **B**: Alluvial fan deposits, comprising poorly consolidated gravels (**a**), coarse to fine grained sand (**b**), with clayey topsoil (**c**). **C**: Typical shallow and wide sinkhole (depth to diameter ratio $D \approx 1.5\,\mathrm{m}/17\,\mathrm{m} = 0.09$) with gentle slopes in the mud-flat deposits about 100 m north of the alluvium/mud-flat contact (**a**). Note tripod for scale. **D**: Listric normal fault bounding outward-rotated blocks of a landslide or slump into a dry stream channel in the rheologically weak mud-flat deposits. **E**: Small overhanging sinkhole in a mud-salt sequence locally dominated by thin but strong evaporite layers. Highlighted by contrast stretching is the wet mud filling. A tunnel has been carved into the strong salt layer whose overhanging side points towards the Dead Sea. **F**: Typical deep sinkhole with high $D = 12\,\mathrm{m}/23\,\mathrm{m} = 0.52$ in the rheologically strong alluvium. **G**: Inward-tilted and overhanging faulted blocks at the margin of a sinkhole in the alluvium. Note person (circled) for scale. **H**: Overhanging side walls of sinkhole in the alluvium, here highlighted by contrast stretching. **I**: Up to 2 m high normal fault scarp (**a**) and ca. 4 m deep cracks (**b**) in the alluvium about 20 m from the alluvium/mud-flat transition (**c**).

16
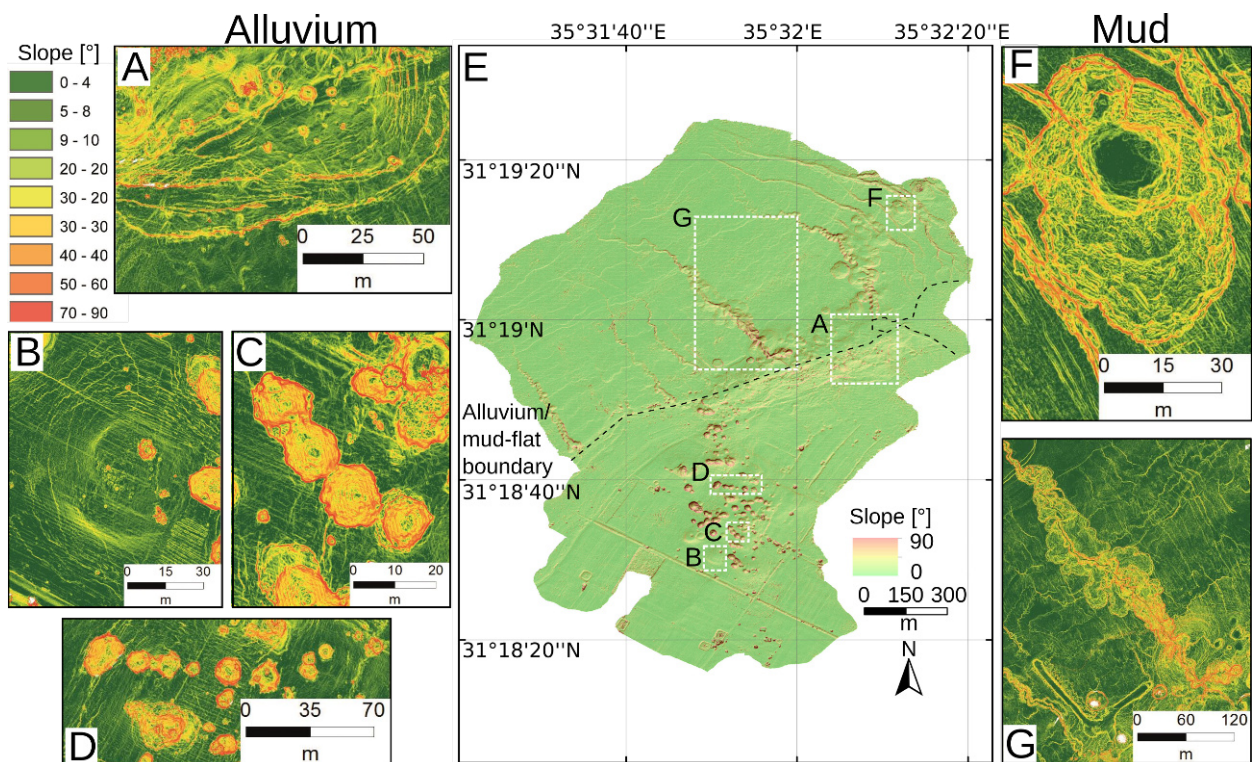
Fig. 11: Slope maps with hillshade background to visualize the morphological expressions of subsidence and depression structures at Ghor Al-Haditha. Slopes in alluvium sinkholes are generally much higher ($> 45\,^\circ$) than in mud. The specific morphological expressions for alluvium (**A-D**) and mud (**F-G**) are described in the text. Note the different colorscale to highlight the detailed structures.

the value is slightly shifted to 8–16 m, with a longer tail due to larger diameters of up to 75 m in the surveyed area. Sinkholes in the alluvium deposits display a higher depth to diameter ratio, ($\bar{D}_a = 0.4 \pm 0.11$) than those in the mud layers ($\bar{D}_m = 0.14 \pm 0.04$; Fig. 12B). The surveyed sinkholes show a mean eccentricity value of $\bar{E} = $ long axis/short axis $= 1.3062 \pm 0.23$, with similar values for for mud $\bar{E}_m = 1.37 \pm 0.24$ and alluvium $\bar{E}_a = 1.28 \pm 0.225$ (Fig. 12C). E values larger than 2 are rarely observed, however.

Sinkholes with $E > 1.05$ on the alluvium display a main orientation of NNW–N, while those in the mud strike NNE–NE (Fig. 13). Nested or elongated sinkholes appear in both types of cover material (see DSM in Fig. 8 and Appendix Figs. A.2B and D). Coalesced or nested sinkholes are considered as one entity if their margins partially overlap. The general trend of all sinkhole long axes is N to NNE. This is because those in the alluvium outnumber those in the mud.

4.5. Surface and subsurface groundwater flow

Typical erosional morphological features observed in the former lake bed are wave-cut steps, rills and both surface and sub-surface stream channels. Wave-cut steps up to 0.75 m high mark former shoreline limits. Erosional rills are generally orientated perpendicular to the mud-flat slope. Most stream channels dissecting the mud-flat (Fig. 7) were dry at the time of our survey. However, several active streams were also observed:

1. A main stream channel (canyon) emerges in the center of the ENE-WSW elongated sec-
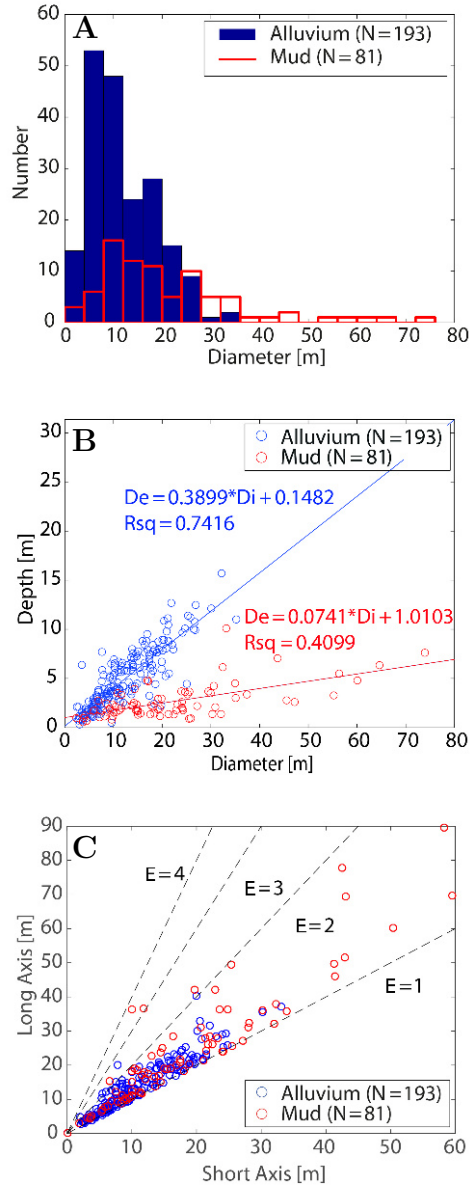
Fig. 12: Quantitative analysis of sinkhole geometries at Ghor Al-Haditha. **A**: Histogram (i.e. frequency-magnitude distribution) of sinkhole diameters in alluvium (blue) and mud (red). **B**: Sinkhole mean diameter to maximum depth. Sinkholes in alluvium material show higher depth/diameter (D) ratios between 0.05 and 1.8 with a mean of 0.4. Sinkholes in mud have values of D between 0.036 and 0.41 with a mean of 0.14. **C**: Plan-view long axis versus short axis plot of all sinkholes in the area. The mean eccentricity is $\bar{E} = 1.306$.
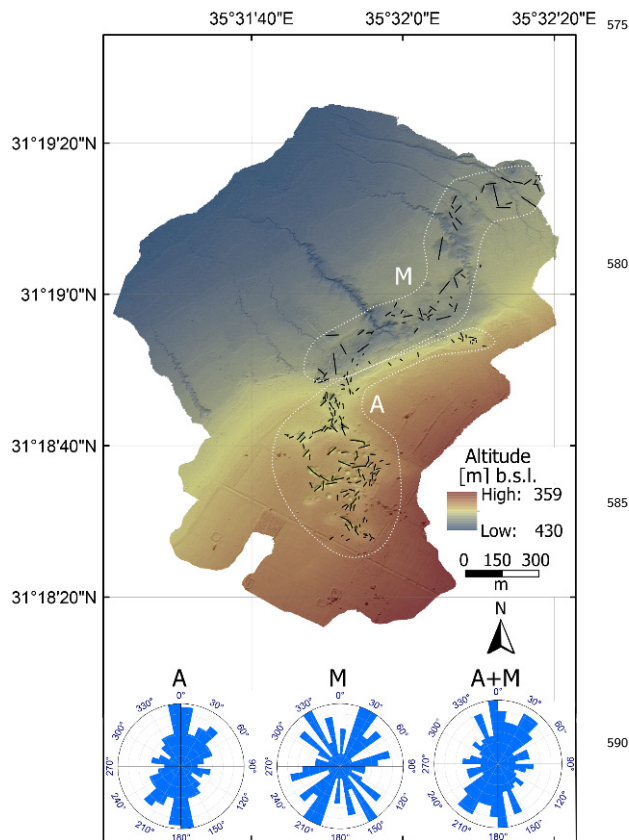
Fig. 13: Map showing the azimuths of the long axis of sinkholes with $E > 1.05$. The rose diagrams at the bottom are produced by a $9\,^{\circ}$ binning for **A**, the alluvial sinkholes, **M** the mud sinkholes and **A+M** all sinkholes. The trends are discussed in the text.

tion of the main depression (Fig. 8). The stream rises from several springs here within the mud-flat sediments at or near the contact with the alluvium. The main spring lies in the channel head at around $6.5 - 7\,\mathrm{m}$ below the former lake bed (Figs. 14A,B). In addition, a spring rises under the now destroyed factory site and feeds a tributary stream that passes through several vegetated pools before joining the main stream. The main stream meanders, with slump related structures on the outer-arc bends and discharges into the Dead Sea. Both the stream channel depth and the marginal slumping gradually diminish lakeward. Aerial images and field observations show that is is carrying a substantial load of sediments already at the spring points (Fig. 14C,E). An artesian, periodically and rapidly location changing, sediment-laden new spring (Fig. 14D,E) formed in 2015, a few tens of meters SE of the main springs of 2014, as observed during a second field survey in October 2015. It disgorges pebbles of the alluvial sequence in the pressurized outflow (Fig. 14E), thus indicating subsurface flow through the alluvium or along the alluvium/mud boundary.

2. A small active stream channel in the North that carries reddish sediments into the lake (close to the location of Fig. 14G). The spring point must lie within the mud-flat as the heads of all channels from the more recent Wadi Mutayl fan were dry.

3. At least one small subsurface stream (Fig. 14F) has been observed at the base of a hole of around $1.5\,\mathrm{m}$ depth in the central area of

19

the mud-flat. No directly obvious outflow of this channel into the Dead Sea could be seen at surface, nor could a surface inflow source be found.

The mud-flat also exhibits several slump-related seeps, as well as water-filled sinkholes that lack salt rims (Fig. 14A) and have no obvious channel connection (Figs. 14H,I). Whether active or dry, several stream channels that cut the mud-flat do not continue onto the alluvium. Rather, the heads of these channels occur at or close to the alluvium/mud-flat boundary (Fig. 7). With the exeption of the Wadi Mutayl at the north-eastern-most edge, there are currently no natural stream channels on the alluvium in the surveyed area. A storm drain runs NW–SE at the SW edge of the surveyed area, but does not continue into any of the stream channels incised into the mud-flat.

Trees and bushes are preferentially found at the old shoreline, particularly where this coincides with the margin of the main depression. They are also found in dried streams on the mud or even inside many sinkholes on the alluvium (Fig. 7). Aerial photos of the current shoreline reveal dark, circular to sub-circular shaped features in clusters immediately off-shore (Fig. 14G), which elsewhere have been associated with submarine sinkholes and springs in coastal karst systems (Fleury et al., 2007; Boever et al., 2013).

4.6. Temporal evolution of surface and groundwater flow from satellite image analysis

Here we take a closer look at the 1970 satellite image presented in Section 2. To highlight vegetation and water channels, we used a coloured version of the image (Fig. 15). Although flow from the Wadi Ibn Hamad is constrained today by engineering works (Fig. 1c), in 1970 flow was dispersed within alluvial fan-deltas that extended both south of and inside todays' sinkhole affected area. In particular, one observes two individual water channels leading from the wadi to the present-day main depression zone. Interestingly, the currently most affected area around the destroyed 'Numeira mixed salts and mud company' factory was located at the outflow points of those two channels at that time.

Publically available satellite images (Google Earth) of the 2000s show the development of a lake of unsaturated water within the current main depression. This lake was separated from the Dead Sea base level by a NE-SW elongated natural dam made of salty mud (Closson and Abou Karaki, 2008), i.e. the NW margin of the main depression. The water accumulated exactly at the boundary between the alluvium and clay sequences.

The evolution of a wide canyon, related to the drainage of the lake, is seen in satellite images (Fig. 16). In an image from March 2012 a NW–SE stream channel terminating landward in a fork has developed from the Dead Sea shore to the middle of the mud-flat. This channel is not visible in an image from December 2011. There is also an outflow point from the lake in the centre of Closeup image (a in Fig. 16), but this cannot be traced with certainty to the fork in the image. It is thus possible that the connection was underground at this time. By retrogressive erosion, the NW–SE stream channel extended towards the lake, crossing the natural dam perpendicularly (b). The surface connection of the channel with the lake was established between May

20
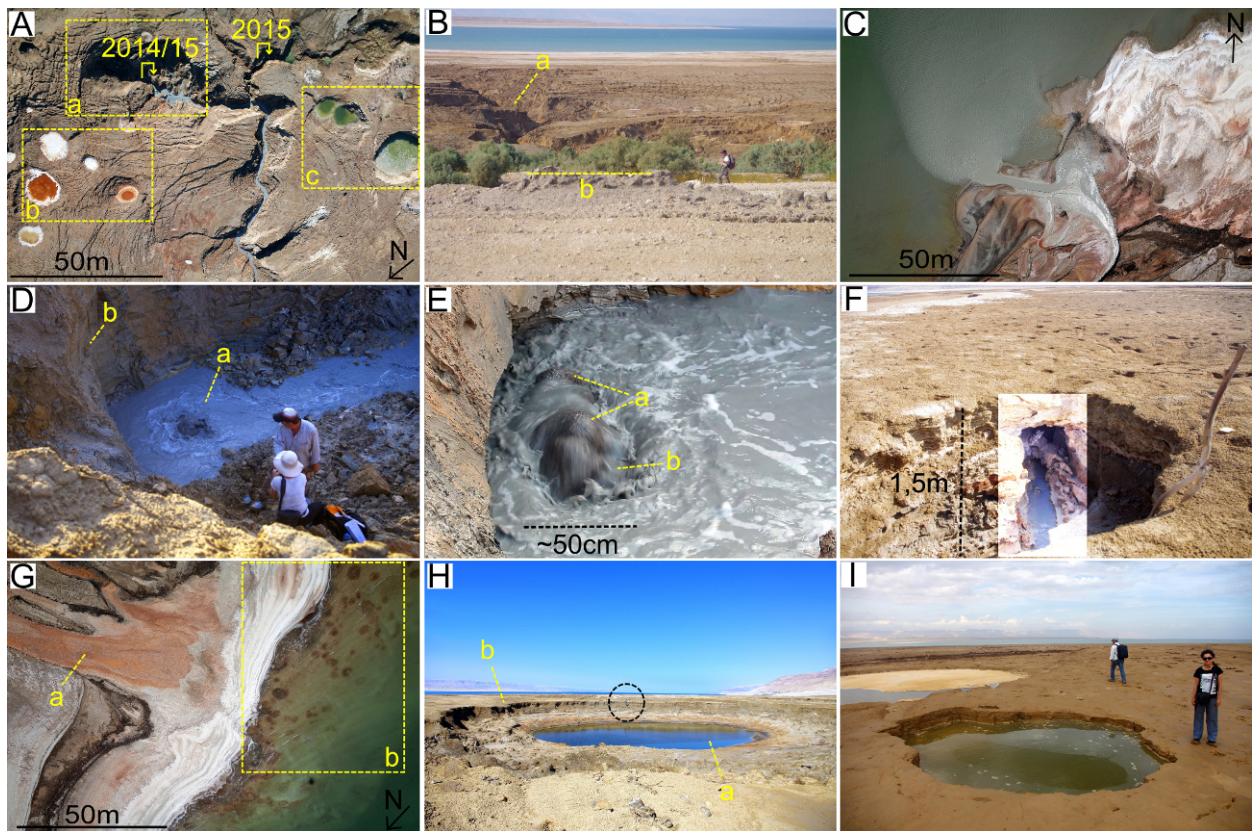
Fig. 14: Evidence of subsurface groundwater flow and subrosion in the mud-flat at Ghor Al-Haditha. **A**: A sediment-laden stream emerging from within the mud-flat sediments (**a**). Clearly distinguishable are sinkholes in the mud-flat filled by saturated salt-water (**b**, note white rims of salt) and fresh/brackish water (**c**). The main springs observed in 2014/15 and the newly formed artesian spring (part D and E) are marked. **B**: Vegetated contact between alluvial fan and mud-flat. The active stream channel in part A has dug a 6–7 m deep canyon into the mud-flat (**a**). Its spring point lies a few tens of meters north of the alluvium/mud-flat contact (**b**). **C**: Sediment plume at the outlet of the active main stream shown in A. **D**: New artesian, periodically location changing and sediment bearing spring (**a**) discovered in Oct. 2015 at the main canyon area. This outflow was observed to cause active upstream channel incision through collapse of overlying material (**b**). **E**: Spring of subfigure D carrying clearly visible sediments (**a**) and pebble-sized clasts (**b**) in the upwelling water. **F**: Channelized flow within the mud-flat sediments. Highlighted by contrast stretching, the water bearing channel has no onshore outflow, hence indicating a submarine point of emanation. **G**: Current Dead Sea shoreline at superficially dry canyon fan-deltas (**a**). Dark round shapes in the water are possibly related to submarine sinkholes and/or springs (**b**). **H**: Fresh-water filled mud-flat sinkhole (**a**) with no obvious surface channel connection, hence indicating subsurface recharge. Freshly collapsed rims show a continuing lateral sinkhole evolution (**b**). Note person circled for scale. **I**: New sinkhole on the mud-flat, formed after a storm event in Oct. 2015 and filled with relatively fresh water.
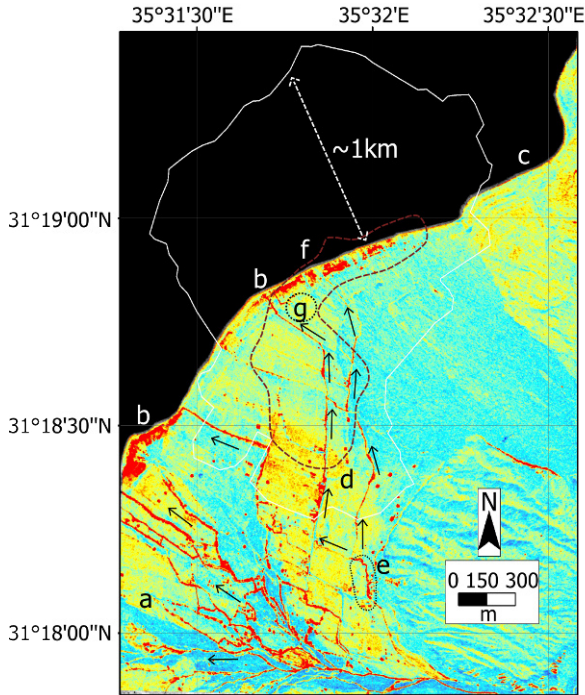
Fig. 15: Coloured Corona image (1970) with close-range photogrammetry outline (2014) highlighting water flow in the Wadi Ibn Hamad delta system (**a**). Vegetation (**b**) at the former Dead Sea shoreline (**c**) appears in red. Two identified main surface water channels (**d**) bifurcate at (**e**) from the Wadi Ibn Hamad. They flow into what is now the main depression zone (**f**) and pass the future Numeira mud factory location (**g**). Interpreted surface water flow is indicated by arrows.

and June 2012 (b and c). Progressive with the development of the channel the reservoir drained, as seen in the receding lake shore line from March to June 2012. By August, the lake was almost completely drained (d). The NW–SE stream enlarged progressively owing to the springs located in the depression. The nearly dried out area comprised several nested depression structures with channels between them in August 2012. By the time of our survey in October 2014, only a few water-filled ponds remained around the factory site.

4.7. Estimation of volume loss due to sub-surface material removal

Under the assumption of stability around the areas obviously affected by subsidence, we are able to calculate an interpolated pre-subsidence DSM (Fig. 6A). From this, a minimum volume loss of the depression and sinkholes can be estimated by GIS volume subtraction algorithms for equally gridded datasets. Only minimum values can be determined by this approach because the margins around the areas of interest might have also subsided and sinkhole refillings are not considered. A compilation of the results for the depression zone in mud and alluvium separately and for the whole surveyed area is presented in Table 2.

The total minimum volume loss of this area including stream channels is estimated as roughly $\Delta V_{min,tot} = 2.5 \cdot 10^6 \, \mathrm{m}^3$. Assuming, the strong Dead Sea recession started in 1955 (cf. Section 2 and Taqieddin et al., 2000) this would mean a minimum erosion rate of $r_{tot} = 41,670 \, \mathrm{m}^3 \, \mathrm{yr}^{-1}$. As sinkholes in the study area only appeared from the year 1990 on, 25 years of subsurface material re-

22
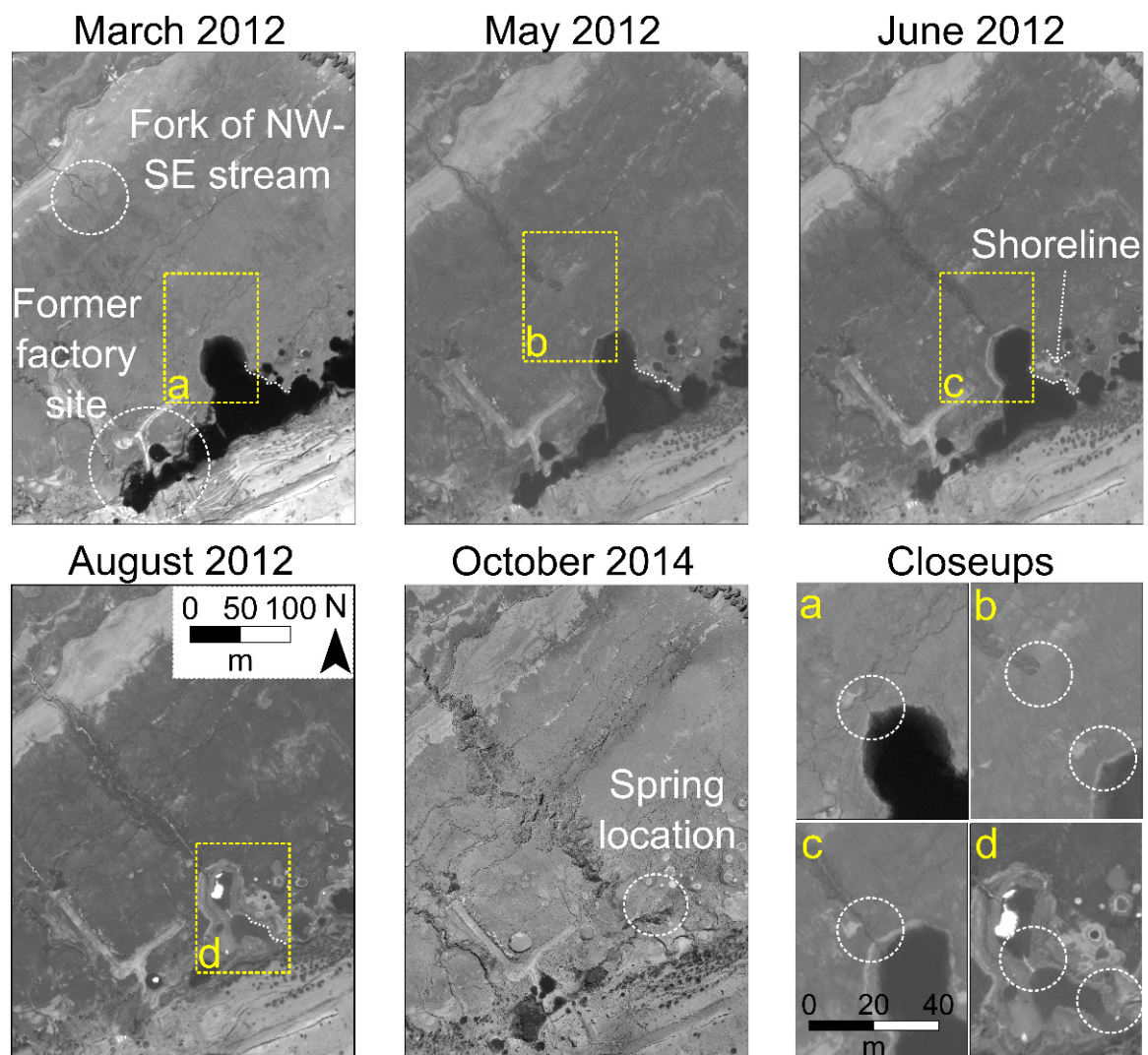
Fig. 16: Lake drainage and canyon development near the former mud factory site. Images were acquired in March (Quickbird-2 with $0.6\,\mathrm{m\,px^{-1}}$ resolution), May, June, August 2012 (Worldview-2 satellite with $0.46\,\mathrm{m\,px^{-1}}$) and October 2014 (orthophoto from close-range photogrammetry). Visible channels (circled) exist already in March 2012 in the NW, where later the canyon develops. Note the shoreline retreat from May to August 2012 as indicated by the dashed line. Circles on closeup figures **a-c** show the lake outflow point and migrating channel head (nick-point) and channels interlinking the lake remnants in **d**.

Table 2: Affected area A, minimum volume loss ΔV_{min} and corresponding minimum average subsidence S_{min} for the alluvium and mud zones of the main depression as well as the total survey area in 25 years.

	alluvium	mud	total
A [km^2]	0.197	0.144	2.1
ΔV_{min} [m^3]	$0.83 \cdot 10^6$	$1 \cdot 10^6$	$2.5 \cdot 10^6$
S_{min} [m]	4.2	6.95	1.2

moval ($\Delta V_{min,dep} = 1.83 \cdot 10^6$ m^3) leads to an estimation of the minimum erosion rate in the main depression area to $r_{dep} = 73,200$ m^3 yr^{-1}.

The minimum subsidence S_{min} is calculated by $S_{min} = \Delta V_{min}/A$ averaged over each area of interest. For the southern part of the depression area in the alluvium the calculation yields $S_{min} = 4.2$ m. For the northern part of the depression area in the mud-flat, including the boundary region to the alluvium with strong topographic gradient (Fig. 8), we have $S_{min} = 6.95$ m. Weighted by the area for alluvium and mud, the total value for the depression area is $S_{min,dep} = 5.36$ m. This yields an average minimum subsidence rate of $\dot{S} = \approx 0.21$ m yr^{-1} for the main depression in 25 years.

5. Discussion

This qualitative and quantitative geomorphological analysis of the sinkhole affected area of Ghor Al-Haditha reveals several main new results. A NNW–NE orientated, 0.34 km^2 gentle depression straddling mud-flat and alluvial-fan sediments contains the majority of nearly 300 sinkholes in the surveyed area.

Sinkhole morphologies depend on the cover material in which they formed: In mud, the holes are elliptically shaped ($\bar{E}_m = 1.37 \pm 0.24$) with a long-axis strike of NNE-NE and a depth to diameter ratio of $\bar{D}_m = 0.14 \pm 0.04$. In alluvium, holes show a similar eccentricity ($\bar{E}_a = 1.28 \pm 0.255$), but with a long-axis strike of NNW–N and $\bar{D}_a = 0.4 \pm 0.11$. Sinkholes have a clustered distribution ($N\bar{N}R = 0.69, \bar{d} = 18.66$ m), with a bulk cluster orientation of NNW–N in alluvium and NE–E in mud and a density of 6.6 sinkholes ha^{-1} in the most affected zone in and around the main depression.

Dynamic, sediment-laden springs appear at the alluvial-fan/mud-flat contact. Channelized subsurface groundwater flow is seen within the salty mud evaporite sequence of the mud-flat. These flows discharge into the Dead Sea either through canyon-like channels or tunnels. Analysis of satellite images reveals the former existence of wadi riverbeds spatially coincident with the main depression on the alluvial fan. The satellite images also reveal that the section of the main depression along the mud-flat/alluvium boundary hosted a lake that drained in conjunction with the development of an upstream incision of a channel. This new canyon-like channel hosts the major active stream in the surveyed area and is fed from springs rising within the main depression.

The calculated minimum volume loss since 1955 in the main depression is $\Delta V_{dep} = 1.83 \cdot 10^6$ m^3, around 73 % of the volume loss of the whole survey area. The surface of the now main depression area lies on average at least 4.2 m in the alluvium and 6.95 m in the mud lower than 25 years ago. This leads to a minimum average subsidence rate of $\dot{S}_{min} \approx 0.21$ m yr^{-1}.

24

After a quality assessment of the DSM, we focus in this section on different aspects of the control of subsidence and sinkhole formation. We provide an overall interpretative scheme and highlight relevant implications for areas and studies of similar natural hazard phenomena.

5.1. Quality and relevance of the DSM and uncertainties in volume loss calculation

This study shows the feasibility of the cost-efficient Helikite aerial survey approach to address complex geomorphological phenomena like subsidence and sinkhole formation at the Dead Sea. It has been shown that the distribution, accuracy and orientation of GCPs rather than the quantity is essential for correct georeferencing. This is important for e.g. planning further photogrammetric surveys in terrains that are hard to access. As some of the GCPs were lost during the survey, their distribution across the area is not homogeneous, introducing a larger reprojection error especially at the margins of the area (cf. Figs. 5 and 6).

Two small artefacts (Fig. 8) are identified in the DSM by careful comparison with the orthophoto (Fig. 7). One artefact is a consecutive topography change that arises from vegetation cover. It is only visible at strong relief shading and is within the margin of error of the vertical accuracy of the DSM. Another artefact appears as an arc-like step and is due to different light conditions of surveys undertaken at different times of day. Data gaps due to missing images occur only at a small (60×30 m) spot in the mud-flat.

Sinkhole mapping has been done carefully with back and forth comparison of DSM and orthophoto to exclude features of human origin, such a irrigation ponds. The maximum depth of small sinkholes with overhanging sides is underestimated because of shadowing effects. This introduces a small error for the D ratio estimation for those holes, but since the number affected is small (4 out of 298), the error has negligible impact on our main conclusions.

The volume loss of the main depression has been calculated under the premise of a non-subsided surroundings (Fig. 6A). We have currently no means of testing the validity of this premise, but there are no grounds to regard it as unreasonable. Nevertheless, such a surface-derived volume loss, for both individual holes and the main depression is likely to be less than the true sub-surface volume loss, because of material dilation during subsidence ('bulking', cf. Reddish and Whittaker, 2012) and possible sinkhole refilling by farmers. We provide a minimum value for the total volume loss and dependent erosion rate and subsidence estimation. This includes stream channels, springs, roads, vegetation and artificial water ponds, although the contribution from these factors is small. The contribution of the main stream channel incision to volume change in the mud-flat area of the main depression is likewise negligible ($\approx 7\%$).

Sinkhole hazard susceptibility models (cf. Galve et al., 2011) generally apply the here presented well-established GIS analysis. Our photogrammetric survey however provides a high resolution DSM for further detailed studies on sinkhole precursors. Subtle local subsidence and crack formation may precede sinkhole collapse processes (Tharp, 1999; Closson et al., 2009; Shalev and Lyakhovsky, 2012), and these are detectable by the InSAR technique

25

(Nof et al., 2013; Intrieri et al., 2015). On a large scale, typical subsidence rates of mm–cm month^{-1} before sinkhole formation have been determined (Baer et al., 2002; Abelson et al., 2006; Yechieli et al., 2015), while on the local scale the low resolution $(2.5\,\mathrm{m\,px}^{-1})$ of the technique and the missing orthophoto for comparison prevents a more detailed analysis (cf. e.g. Intrieri et al., 2015). This gap can be filled by low-altitude UAV surveys such as performed here. Our approach can be used either as a stand-alone method, or in combination with subsurface investigation via geophysical (e.g. Kaufmann et al., 2011; Margiotta et al., 2012; Kaufmann, 2014), hydrogeological (e.g. Caramanna et al., 2008; Panno et al., 2013) and numerical modeling methods (e.g. Shalev et al., 2006; Fuenkajorn and Archeeploha, 2010; Lollino et al., 2013). Given the high resolution, the simple application (especially in areas of complicated legal permissions) and the cost-efficiency both of the equipment and logistics, a similar approach may be appropiate for scientific research and early-warning analysis in other subsidence and sinkhole affected regions worldwide.

5.2. Lithological control on subsidence structure and morphology

Our quantitative sinkhole depth/diameter analysis confirms results of previous studies elsewhere around the Dead Sea, in that we also show that sinkhole morphology is strongly controlled by the differing mechanical properties of the sediments in which they form (e.g. Arkin and Gilat, 2000; Filin et al., 2011; Shalev and Lyakhovsky, 2012). The soft, cohesive clay sequence reveals a dominant 'sagging style' subsidence. This suggests the role of

a mechanically weaker cover material in the depression formation (Holohan et al., 2011; Shalev and Lyakhovsky, 2012). A related brittle-ductile deformation leads to the formation of wide but shallow sinkholes which enlarge laterally by retrogressive slumps. As seen in numerical models (cf. Holohan et al., 2011), this process of lateral enlargement in the weak mud probabaly accounts for the observed wide periphal zones of fractured and outward-rotated blocks around many sinkholes in the mud. It may also explain both the low depth/diameter ratio and skew towards larger diameters seen for sinkholes in the mud (cf. Fig. 12).

The alluvial fan sediments show generally poor cementation and so are generally easily erodible (Taqieddin et al., 2000). Compared to the mud however, the alluvium is rheologically rather strong, and supports a more brittle deformation style. The older alluvium is locally sufficiently compacted/cemented to form vertical scarps of up to 2 m in height and cracks of up to 4 m deep, bordering the main depression. Moreover, the alluvium enables sinkholes within it to attain generally higher slopes and greater depths than the mud. In some cases alluvial-based sinkholes have overhanging sides and cavities have also been observed (Closson and Abou Karaki, 2009). Similar features also characterise sinkholes formed in salt-dominated deposits at the surface. These structural and morphological characteristics of subsidence are seen also in numerical models with high material strength (Holohan et al., 2011). The high strength of the alluvium retards the lateral enlargement of the sinkholes, thus leading to the observed higher depth/diameter ratio (cf. Fig. 12).

5.3. Structural controls on sinkhole distribution and alignment

A structural control by NNE trending concealed neotectonic faults is suggested by Closson and Abou Karaki (2009) to be such a preferred groundwater flow and material dissolution path, responsible for the typically observed clustering and alignment of sinkholes along an en-echelon structure. We find a general northward trend of the sinkhole long-axis alignment, which only in the mud sinkholes partially matches the general major Dead Sea rift faults' N10–30° trend. On the other hand, long-axis azimuths (NNW–N) in the alluvium point towards the former mud factory. They are similar to fregional fault strikes determined by Diabat (2005) in the hard rock areas around Ghor Al-Haditha.

No direct evidence of tectonic faults or fractures has been found in the surveyed area, although these may be concealed (Closson, 2004). Cracks, crevasses and faults adjacent to the main depression zone are spatially and temporally linked to it, and so are non-tectonic (i.e. local subsidence-related structures). With continuous base-level drop, the former surface water channels revealed by the satellite image analysis (Section 4.6), are very likely to still persist as preferential pathways deeper in the underground. The main depression, and hence the distribution of the sinkholes and their appearance in clusters, at least on the surveyed scale, depends strongly on the distribution of salty mud-flat deposits (bathymetry and shore-line geometry) and the subsurface-water channel flow directions from the main wadis Ibn Hamad and Mutayl.

Due to the limited size of the survey area, we cannot rule out that the groundwater flows reveal concealed tectonic faults at a regional scale, e.g. for the bulk cluster orientation (Closson and Abou Karaki, 2009). However, in light of our results we suggest for the local scale at the survey area in Ghor Hadith a sub-surface stream flow control on subsidence and clustered sinkhole distribution. Tectonic faults are not necessary to explain the observed groundwater flow when we consider a developing karst aquifer system, as we will illustrate in the following section.

5.4. Sinkhole formation by dissolution/subrosion in a karst aquifer

The clay sequence of the former Dead Sea lake bed is considered as an aquiclude (Bender, 1968; Frumkin et al., 2011; Mallast et al., 2011; Ezersky and Frumkin, 2013; Siebert et al., 2014c), sub-dividing the alluvium into several sub-aquifers (Shalev et al., 2006; Yechieli et al., 2015) and hence preventing direct groundwater flow except when subject to faulting. We have shown from field and satellite observations in Section 4.6, however, that the mud sequence allows direct groundwater penetration, as stated originally in Arkin and Gilat (2000). Our direct field observations include: (1) channelized subsurface water flow and seepage within the upper few meters of the interlayered salt and mud succession; (2) sinkholes with fresh/brackish water in the mud-flat without any associated surface channel and (3) the emergence of partly artesian springs within the mud-flat (cf. Section 4.5). It is reasonable therefore to consider that a karst aquifer is developing inside the salt and mud deposits of the mud-flat area. We hence interpret the current behaviour of the Dead Sea mud at Ghor

27

Al-Haditha in hydrogeologic terms as aquitard, i.e. hindering groundwater flow but not preventing it.

We propose that the combination of chemical dissolution/leaching of the carbonate and salt minerals in the mud (cf. Section 4.4) and mechanical mobilization (subrosion) of poorly consolidated lacustrine and alluvial sediments (cf. Section 4.5) increases the permeability of the subsurface. A layered interface model among fresh-water (7–20 m depth), a mixing zone (20–32 m), saline water (32–81 m) and Dead Sea water (from 81 m depth) has been established by Alrshdan (2012) based on transient electromagnetics and electric resisitivity imaging results on the alluvium close to the former mud factory. Due to the decreased base-level by ca. 18 m since 1999, the hydraulic gradient from the Wadi Ibn Hamad to the Dead Sea is expected to be even stronger than $> 30 \, \mathrm{m \, km^{-1}}$ as determined by Sawarieh et al. (2000) (Fig. 2). Such a hydrogeological setting of a strong base-level drop, radially flowing groundwater towards the Dead Sea, high evaporation rates (cf. e.g. Salameh and El-Naser, 2000; Salameh and Hammouri, 2008; Siebert et al., 2014b; Salameh, 2016), sudden potentiometric differences and transient hydraulic head (at Ghor Al-Haditha: periodic wadi flood events) offers ideal conditions for the development of a karst system of branchwork caves (cf. e.g. computer models by Kaufmann and Braun, 2000; Gabrovšek et al., 2014) and sinkhole clusters (Whitman et al., 1999; Denizman, 2003). Additionally the local existence of rheologically strong evaporite layers in the mud (cf. Section 4.4) supports tunnel and subsurface void formation (cf. Section 5.2). This enables a positive feedback loop between cavity/channel creation

and focussed groundwater flow. Consequently, the salty-mud deposits of the former lake bed may undergo a transition from initial aquiclude behaviour to progressively less-effective aquitard behaviour.

Such a process of relatively fast karst formation is highlighted in a conceptual model for Ghor Al-Haditha in Fig. 17. It is based not only on findings of this study, but also on (hydro)-geological information (boreholes) from El-Isa et al. (1995); Sawarieh et al. (2000); Taqieddin et al. (2000) and recent studies from Krawczyk et al. (2015) and Polom et al. (2016), which delineate the subsurface mud/alluvium boundary via shear wave reflection seismics.

Our quantitative sinkhole results (NNR, depth/diameter, eccentricity) fit well with outcomes of GIS studies in limestone karst (e.g. Whitman et al., 1999; Denizman, 2003), evaporite karst (Galve et al., 2009; Gutiérrez and Lizaga, 2016; Gutiérrez et al., 2016) and previous studies at the Dead Sea (Filin et al., 2011). All have in common that sinkholes appear clustered, with a higher frequency of small diameter sinkholes and pronounced elongated geometry. Because of the high sinkhole density of $6.6 \, \mathrm{sinkholes \, ha^{-1}}$ and high degree of clustering, the nearest neighbor distance is at the lower margin of the study of Denizman (2003). This possibly indicates a youthful to early mature stage of a salt karst according to the engineering classification (cf. e.g. Waltham, 2016).

On the western side of the Dead Sea, the documented sinkholes, subsidence, uvalas and submarine springs (cf. e.g. Siebert et al., 2014b; Yechieli et al., 2015) are typical earth surface expressions of such a developing karst system (cf. e.g. Benito

et al., 1995; Goldscheider and Drew, 2007; Parise, 2010). A 2–20 m thick and $20-50$ m deep salt-layer from the Holocene period is found on the western side of the Dead Sea at Ein Gedi, nearby Mineral Beach and Nahal Hever (Fig. 1B, cf. e.g. Abelson et al., 2006; Ezersky, 2008; Legchenko et al., 2008; Ezersky et al., 2009; Stein et al., 2010; Frumkin et al., 2011; Yechieli et al., 2015). Evidence of such a thick salt-layer at Ghor Al-Haditha (El-Isa et al., 1995; Taqieddin et al., 2000; Ezersky et al., 2013) is relatively weak (Polom et al., 2016), although we cannot rule out its existence. Hence the subsidence phenomena can be alternatively explained by the progressive kartification of the thinly-bedded salty mud deposits with subsequent or concurrent physical material removal (subrosion) in the alluvium (Fig. 17A).
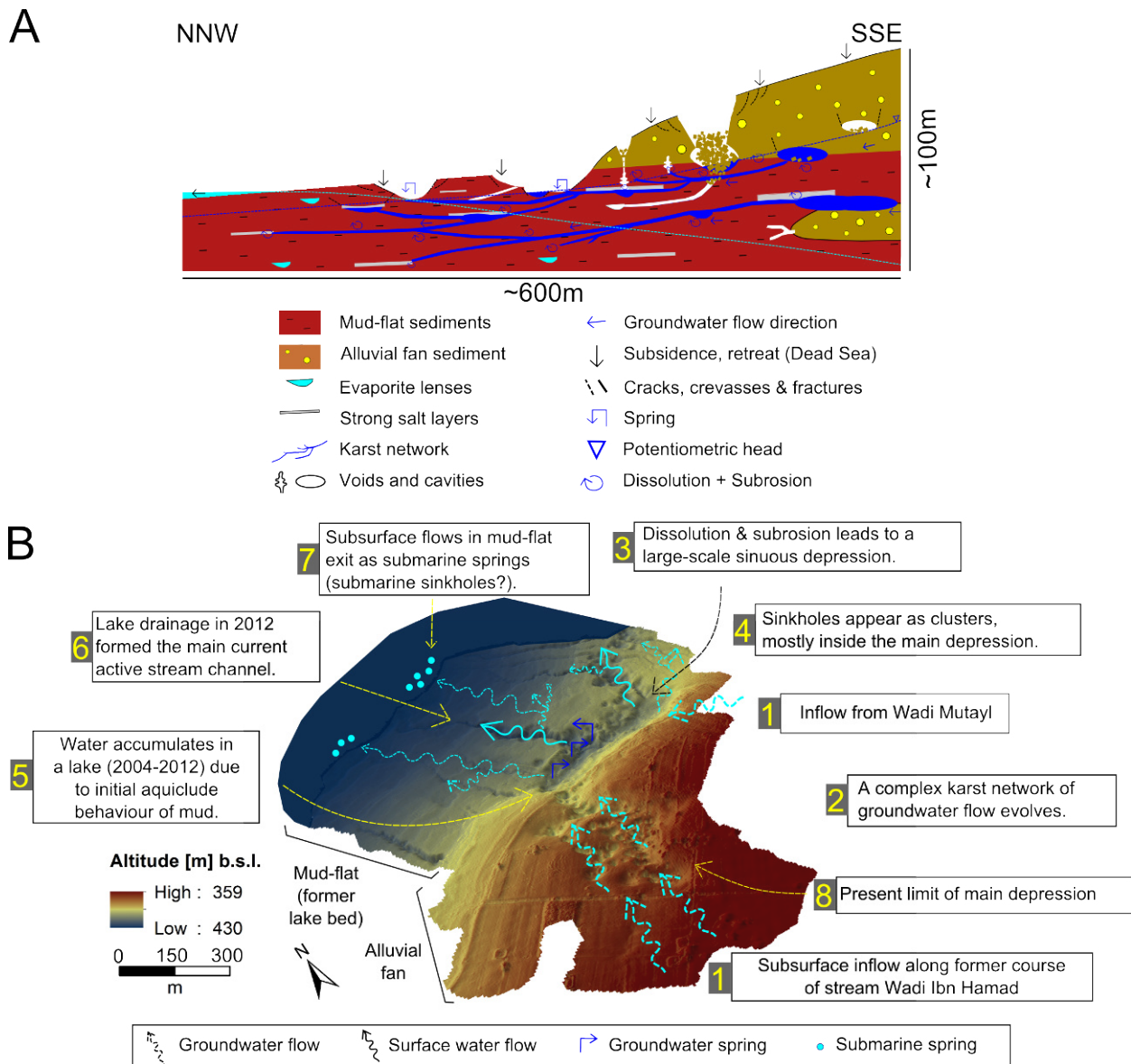
A similar mechanism of sinkhole formation by subsurface drainage and flow is mentioned by Arkin and Gilat (2000); Filin et al. (2011) and Garfunkel and Ben-Avraham (1996) on the nearby Lisan peninsula and at several sites on the western side. Therefore this mechanism - the Dead Sea mud acting as an aquitard and later as an aquifer - poses also a scientific novelty for numerical modeling of sinkhole formation including groundwater flow (see Shalev et al., 2006; Ezersky et al., 2013), and should be considered in further studies at both sides of the Dead Sea.

5.5. Overall interpretation of land subsidence at Ghor Al-Haditha

Our overall interpretation of the development of land subsidence and sinkhole formation processes at Ghor Al-Haditha is depicted graphically in part B of the conceptual model of Fig. 17.

Groundwater flows lakeward beneath the alluvial cover, following the old stream paths of waters from Wadi Ibn Hamad and Wadi Mutayl, seen in the satellite image from 1970 (Fig. 15). The subsurface sequences of intercalated alluvial fans and mud-flat sediments containing thin evaporite layers can easily be chemically and mechanically removed by the undersaturated water flow, which is driven by the high hydraulic gradient due to the continuous base-level drop. Sinkhole clusters appear initially on the alluvium but also later on the mud-flat (cf. Section 4.1). At the confluence of the groundwater flows and at the boundary between alluvium and mud-flat, a large depression formed with concentric cracks around it. The mud-flat sediments here act as an aquitard, leading to an accumulation of water in the depression to form major lakes and appearance of partially artesian springs (Fig. 17A). The lake drains, as a large canyon is formed via surface and subsurface flow in the exposed mud-flat on a timescale of a few months (cf. Section 4.5). The mud progressively develops into a karst aquifer system depending on the distribution of evaporites. Sinkholes nowadays appear more and more in the N–NE of the main depression, hence indicating a direction of the hydraulic gradient with the clayey layers as initial limiting boundary conditions. Subsurface channels without observed outflow into the Dead Sea are found and are likely to terminate as submarine springs. This system of preferential subterranean groundwater flow paths, involving dissolution of evaporitic minerals and subrosion of unconsolidated material, has to be considered as a complex karst water flow network.

A NNW / SSE / ~100m / ~600m

	Mud-flat sediments	←	Groundwater flow direction
	Alluvial fan sediment	↓	Subsidence, retreat (Dead Sea)
	Evaporite lenses	↘↙	Cracks, crevasses & fractures
	Strong salt layers		Spring
	Karst network	▽	Potentiometric head
	Voids and cavities		Dissolution + Subrosion

B

7 — Subsurface flows in mud-flat exit as submarine springs (submarine sinkholes?).

3 — Dissolution & subrosion leads to a large-scale sinuous depression.

6 — Lake drainage in 2012 formed the main current active stream channel.

4 — Sinkholes appear as clusters, mostly inside the main depression.

5 — Water accumulates in a lake (2004-2012) due to initial aquiclude behaviour of mud.

1 — Inflow from Wadi Mutayl

2 — A complex karst network of groundwater flow evolves.

8 — Present limit of main depression

1 — Subsurface inflow along former course of stream Wadi Ibn Hamad

Altitude [m] b.s.l. / High : 359 / Low : 430 / 0 150 300 m

Mud-flat (former lake bed) / Alluvial fan

Groundwater flow / Surface water flow / Groundwater spring / Submarine spring

Fig. 17: Conceptual model of subsidence and sinkhole formation at Ghor Al-Haditha based on findings of this study and of previous investigations by (El-Isa et al., 1995; Sawarieh et al., 2000; Taqieddin et al., 2000; Krawczyk et al., 2015; Polom et al., 2016, partly unpublished reports). **A**: Development of a karst aquifer in the alluvium and clay-sequence along a roughly SSE–NNW cross-section. The geologic sequence consists of interbedded alluvial fan sediments and the lacustrine, evaporite rich mud-flat with strong salt-layers that support tunnels. Dissolution of local evaporitic lenses/layers and salt minerals weakens the material compound. The Dead Sea base-level drop forces strong mechanical mobilization (subrosion) of both mud and alluvial sediments by fresh-water flow and progressive karstification and consequent subsidence/sinkhole formation. Note that subrosion may act even below the salt-water table (light blue line) which is constrained by calculations from Salameh and El-Naser (2000). **B**: Interpretative scheme of subsidence and sinkhole formation processes at the study area, using a 3D Raster topographic image to highlight the main central sinuous depression.

30

Considering the complexity of the subsidence and sinkhole formation process around the Dead Sea, it is clear that a simple interpretative scheme does not explain every single feature or the complete time development in this area. We have studied in detail about $1.5\,\text{km}$ of a $6\,\text{km}$ long sinkhole lineament, hence our findings concern only about $25\,\%$ of the longest sinkholes' lineament in the whole Dead Sea area. In general the hydrogeological conditions, for example the aquicludal behaviour of the Dead Sea mud, the role of the salt-fresh water boundary in a context of such a complex flow network and the existence or removal of a salt-layer, need to be investigated more in detail as they are beyond the scope of this work.

Nevertheless, our results provide a new perspective on the ongoing processes of land subsidence at Ghor Al-Haditha. Importantly, the high resolution DSM and orthophoto, combined with future survey repetitions, will lead to an estimation of short-term subsidence rates (cf. Section 5.1), changes in morphology and the time evolution of sinkhole formation. This will in turn help to delineate zones prone to future collapse inside this actively subsiding area on a very detailed scale.

6. Conclusions

In this work we presented a first high resolution ($5\,\text{cm}\,\text{px}^{-1}$) digital surface model and orthophoto ($6.7\,\text{cm}\,\text{px}^{-1}$) for the sinkhole area of Ghor Al-Haditha in the SE part of the Dead Sea. We showed that the equal dispersed distribution of ground control points in the survey area is of crucial importance for correct georeferencing and reliable subsequent DSM analysis. The high resolution DSM and geomorphological analysis are of high relevance for subsidence and sinkhole hazard and precursor assessment on the eastern coast of the Dead Sea. This photogrammetric study, combined with field and satellite image analysis, reveals new quantative and qualitative aspects of the subsidence and sinkhole formation. We summarize the main outcomes here as follows:

1. A subtle, large-scale (length $1.5\,\text{km}$, width 0.15–$0.4\,\text{km}$), sinuousoidal depression bound partly by non-tectonic faults and orientated NNW with a shift to NE at the mud/alluvium contact has been identified at Ghor Al-Haditha. This depression contains around $85\,\%$ of the almost 300 identified sinkholes spread over $0.45\,\text{km}^2$ of the $2.1\,\text{km}^2$ survey area. Sinkhole density in the most affected zone is $6.6\,\text{sinkholes}\,\text{ha}^{-1}$.

2. The estimated minimum volume loss of the surveyed area is $2.5\cdot10^6\,\text{m}^3$, the main depression alone counts for $1.83\cdot10^6\,\text{m}^3$. The estimated minimum erosion rates are $41,670\,\text{m}^3\,\text{yr}^{-1}$ and $73,200\,\text{m}^3\,\text{yr}^{-1}$ respectively. The minimum subsidence of the depression lies between $4.2\,\text{m}$ (alluvium) and $6.95\,\text{m}$ (mud-flat), with an average subsidence rate of $0.21\,\text{m}\,\text{yr}^{-1}$ since the beginning of sinkhole formation.

3. Sinkholes in the depression area show different morphologies related to the mechanical strength of the materials they formed in. In mud, wide and shallow sinkholes develop with low depth to diameter values (0.14); in alluvium, deep and narrow sinkholes develop (0.4).

31

4. Sinkholes are mostly elliptical with eccentricities of 1.31. The sinkhole sequence shows a significantly clustered distribution with a nearest neighbor ratio 0.69. Long-axis strike of the individual sinkholes in alluvium is between NNW–N, in mud NNE–NE.

5. Springs and highly mobile channelized groundwater flow appear at or near the contact between the mud and alluvium sequences. Observations of entrainment of unsoluble sediments of up to pebble size at the partially artesian springs adjacent this contact suggest that subrosion acts as a significant driving physical process for subsurface material depletion. The Dead Sea mud acts as an aquitard, locally penetrated by solution-driven water channels, which dynamically form new canyon systems and generally follow preferential flow paths.

6. Interbedded evaporite layers of observed 1.5 m maximum thickness facilitate groundwater penetration and dissolution processes within the salty mud sediments of the former Dead Sea lake bed. The voids and conduits form an actively evolving, complex karst system with sinkholes, subsidence and uvalas as typical morphological expressions.

7. A satellite image from 1970 reveals formerly existing surface water streams from the Wadi Ibn Hamad into todays' most affected sinkhole zone. Despite engineering diversion of the river, inferred continued existence of such a preferential subsurface flow provides a basis for chemical and mechanical material removal in the surveyed area.

In conclusion, sinkhole formation and subsidence at Ghor Al-Haditha is related to karstification by both chemical dissolution and mechanical subrosion along a channelized subterranean flow network in thinly interbedded salt and mud deposits. This constitutes an alternative to the massive salt layer dissolution models as proposed formerly for both sides of the Dead Sea.

References

Abelson, M., Yechieli, Y., Crouvi, O., Baer, G., Wachs, D., Bein, A., Shtivelman, V., 2006. Evolution of the Dead Sea sinkholes. In: Enzel, Y., Agnon, A., Stein, M. (Eds.), New Front. Dead Sea Paleoenviron. Res. Geol. Soc. Am. Spec. Pap. 401, p. 241-253. Geological Society of America.

Agisoft, 2013. Agisoft PhotoScan user manual. Professional edition, version 1.0.0.

Al-Omari, A., Salman, A., Karablieh, E., 2014. The Red Dead Canal project: An adaptation option to climate change in Jordan. Desalin. Water Treat. 52 (13-15), 2833–2840.

Al-Ruzouq, R., Al-Zoubi, A., Abueladas, A., Akkawi, E., 2011. Hazard Mapping Along the Dead Sea Shoreline. In: FIG Work. Week - Bridg. Gap between Cult. Marrakech, Morocco.

Al-Zoubi, A. S., Abueladas, A. E.-R. a., Al-Rzouq, R. I., Camerlynck, C., Akkawi, E., Ezersky, M. G., Z.S.H, A.-H., Ali, W., Rawashdeh, S. A., 2007. Use of 2D Multi Electrodes Resistivity Imaging for Sinkholes Hazard Assessment along the Eastern Part of the Dead Sea, Jordan. Am. J. Environ. Sci. 3 (4), 230–234.

Alrshdan, H., 2012. Geophysical Investigations of Ghor Haditha Sinkholes, Jordan. In: 74th EAGE Work. Dead Sea Sink. - Causes, Eff. Solut. Copenhagen, Denmark.

Arkin, A., Gilat, Y., 2000. Dead Sea sinkholes an ever-developing hazard. Environ. Geol. 39 (7).

Atzori, S., Antonioli, A., Salvi, S., Baer, G., 2015. InSAR-based modeling and analysis of sinkholes along the Dead Sea coastline. Geophys. Res. Lett. 42, 8383–8390.

Baer, G., Schattner, U., Wachs, D., Sandwell, D., Wdowinski, S., Frydman, S., 2002. The lowest place on Earth is

subsiding - An InSAR (interferometric synthetic aperture radar) perspective. Geol. Soc. Am. Bull. 114 (1), 12–23.

Beck, B., 2012. Soil Piping and Sinkhole Failures. In: White, W. B., Culver, D. (Eds.), Encycl. caves. Elsevier, New York, pp. 718–723.

Begin, Z. B., Ehrlich, A., Nathan, Y., 1974. Lake Lisan: the Pleistocene precursor of the Dead Sea. Geol. Surv. Isr. Bull. 63, 30 pp.

Bender, F., 1968. Geologie von Jordanien. Gebrüder Bornträger - Berlin - Stuttgart.

Benito, G., del Campo, P. P., Gutiérrez-Elorza, M., Sancho, C., 1995. Natural and human-induced sinkholes in gypsum terrain and associated environmental problems in NE Spain. Environ. Geol. 25 (3), 156–164.

Bentor, Y., 1961. Some geochemical aspects of the Dead Sea and the question of its age. Geochim. Cosmochim. Acta 25, 239–260.

Boever, M. D., Khlosi, M., Delbecque, N., Pue, J. D., Ryken, N., 2013. Desertification and Land Degradation - Processes and Mitigation. UNESCO Chair of Eremology, Ghent, Belgium.

Bowman, D., Svoray, T., Devora, S., Shapira, I., Laronne, J. B., 2010. Extreme rates of channel incision and shape evolution in response to a continuous, rapid base-level fall, the Dead Sea, Israel. Geomorphology 114 (3), 227–237.

Brinkmann, R., Parise, M., Dye, D., 2008. Sinkhole distribution in a rapidly developing urban environment: Hillsborough County, Tampa Bay area, Florida. Eng. Geol. 99 (3-4), 169–184.

Burner, A., Snow, W., Goad, W., 1983. Close-Range Photogrammetry with video cameras. Tech. rep., NASA Langley Research Center, Hampton, VA, United States.

Caramanna, G., Ciotoli, G., Nisio, S., 2008. A review of natural sinkhole phenomena in Italian plain areas. Nat. Hazards 45 (2), 145–172.

Closson, D., 2004. Structural control of sinkholes and subsidence hazards along the Jordanian Dead Sea coast. Environ. Geol. 47 (2), 290–301.

Closson, D., Abou Karaki, N., 2008. Human-induced geological hazards along the Dead Sea coast. Environ. Geol. 58 (2), 371–380.

Closson, D., Abou Karaki, N., 2009. Salt karst and tectonics: sinkholes development along tension cracks between parallel strike-slip faults , Dead Sea , Jordan. Earth Surf. Process. Landforms 34, 1408–1421.

Closson, D., Abou Karaki, N., 2013. Sinkhole hazards prediction at Ghor Al Haditha, Dead Sea, Jordan: "Salt Edge" and "Tectonic" models contribution - a rebuttal to Geophysical prediction and following development sinkholes in two Dead Sea areas, Israel and Jordan", by: Ezersky et all., 201. Environ. Earth Sci. 70 (6), 2919–2922.

Closson, D., Abou Karaki, N., 2015. Earthen Dike Leakage at the Dead Sea. In: Lollino, G., Manconi, A., Guzzetti, F., Culshaw, M., Bobrowsky, P., Luino, F. (Eds.), Eng. Geol. Soc. Territ. - Vol. 5. Springer International Publishing, pp. 461–464.

Closson, D., Abou Karaki, N., Hallot, F., 2009. Landslides along the Jordanian Dead Sea coast triggered by the lake level lowering. Environ. Earth Sci. 59 (7), 1417–1430.

Closson, D., Abou Karaki, N., Pasquali, P., Riccardi, P., 2013. A 300m-width sinkhole threatens the stability of the embankment of a saltpan in Jordan, Dead Sea Region. Geophys. Res. Abstr. 15, 2363.

Dahm, T., Heimann, S., Bialowons, W., 2011. A seismological study of shallow weak micro-earthquakes in the urban area of Hamburg city, Germany, and its possible relation to salt dissolution. Nat. Hazards 58 (3), 1111–1134.

De Smith, M. J., Goodchild, M. F., Longley, P., 2015. Geospatial analysis: a comprehensive guide to principles, techniques and software tools, url=http://www.spatialanalysisonline.com.

Denizman, C., 2003. Morphometric and spatial distribution parameters of karstic depressions, lower Suwanee River basin, Florida. J. Cave Karst Stud. 65 (1), 29–35.

Diabat, A. A., 2005. Sinkholes related to Tectonic Factor at Ghor Al Haditha Area, Dead Sea/Jordan. Hydrogeol. und Umwelt 33 (17), 4.

Doctor, D. H., Young, J. A., 2013. An evaluation of automated GIS tools for delineating karst sinkholes and closed depressions from 1-meter LiDAR-derived digital elevation data. In: Thirteen. Multidiscip. Conf. Sink. Eng. Environ. Impacts Karst. pp. 449–458.

Dreybrodt, W., 2012. Processes in karst systems: physics, chemistry and geology. Vol. 4. Springer Science & Business Media.

El-Isa, Z., Rimawi, O., Jarrar, G., Abou Karaki, N., Taqied-

din, S., Atallah, M., Seif El-Din, N., Al Saed, A., 1995. Assessment of the hazard of subsidence and sinkholes in Ghor Al-Haditha area. Tech. rep., University of Jordan, Center for consultation, technical services and studies.

Esri, 2015. ArcGIS Version 10.2 online resource, url=https://doc.arcgis.com/en/arcgis-online, date accessed 2015-08-13.

Ezersky, M., 2008. Geoelectric structure of the Ein Gedi sinkhole occurrence site at the Dead Sea shore in Israel. J. Appl. Geophys. 64 (3-4), 56–69.

Ezersky, M., Frumkin, A., 2013. Fault - Dissolution front relations and the Dead Sea sinkhole problem. Geomorphology 201, 35–44.

Ezersky, M., Legchenko, A., Camerlynck, C., Al-Zoubi, A., 2009. Identification of sinkhole development mechanism based on a combined geophysical study in Nahal Hever South area (Dead Sea coast of Israel). Environ. Geol. 58 (5), 1123–1141.

Ezersky, M. G., Eppelbaum, L. V., Al-Zoubi, A., Keydar, S., Abueladas, A., Akkawi, E., Medvedev, B., 2013. Geophysical prediction and following development sinkholes in two Dead Sea areas, Israel and Jordan. Environ. Earth Sci. 70 (4), 1463–1478.

Ezersky, M. G., Eppelbaum, L. V., Al-Zoubi, A., Keydar, S., Abueladas, A.-R., Akkawi, E., Medvedev, B., 2014. Comments to publication of D. Closson and N. Abu Karaki "Sinkhole hazards prediction at Ghor Al Haditha, Dead Sea, Jordan: "Salt Edge" and "Tectonic" models contribution - a rebuttal to "Geophysical prediction and following development ...". Environ. Earth Sci. 71 (4), 1989–1993.

Farr, T. G., Rosen, P. A., Caro, E., Crippen, R., Duren, R., Hensley, S., Kobrick, M., Paller, M., Rodriguez, E., Roth, L., Seal, D., Shaffer, S., Shimada, J., Umland, J., Werner, M., Oskin, M., Burbank, D., Alsdorf, D. E., 2007. The shuttle radar topography mission. Rev. Geophys. 45 (2), 1–43.

Filin, S., Baruch, A., Avni, Y., Marco, S., 2011. Sinkhole characterization in the Dead Sea area using airborne laser scanning. Nat. Hazards 58 (3), 1135–1154.

Fleury, P., Bakalowicz, M., de Marsily, G., 2007. Submarine springs and coastal karst aquifers: A review. J. Hydrol. 339 (1-2), 79–92.

Förstner, W., Wrobel, B., 2013. Mathematical concepts in photogrammetry. In: McGlone (Ed.), Man. Photogramm., 6th Edition. American Society of Photogrammetry and Remote Sensing, Bethesda, MD, USA, pp. 63–233.

Frumkin, A., Ezersky, M., Al-Zoubi, A., Akkawi, E., Abueladas, A.-R., 2011. The Dead Sea sinkhole hazard: Geophysical assessment of salt dissolution and collapse. Geomorphology 134 (1-2), 102–117.

Frydman, S., Charrach, J., Goretsky, I., 2008. Geotechnical properties of evaporite soils of the Dead Sea area. Eng. Geol. 101 (3-4), 236–244.

Fuenkajorn, K., Archeeploha, S., 2010. Prediction of cavern configurations from subsidence data. Eng. Geol. 110 (1-2), 21–29.

Furukawa, Y., Ponce, J., 2010. Accurate, dense, and robust multiview stereopsis. IEEE Trans. Pattern Anal. Mach. Intell. 32 (8), 1362–1376.

Gabrovšek, F., Häuselmann, P., Audra, P., 2014. 'Looping caves' versus 'water table caves': The role of base-level changes and recharge variations in cave development. Geomorphology 204, 683–691.

Galve, J., Gutiérrez, F., Remondo, J., Bonachea, J., Lucha, P., Cendrero, A., 2009. Evaluating and comparing methods of sinkhole susceptibility mapping in the Ebro Valley evaporite karst (NE Spain). Geomorphology 111 (3-4), 160–172.

Galve, J. P., Remondo, J., Gutiérrez, F., 2011. Improving sinkhole hazard models incorporating magnitude-frequency relationships and nearest neighbor analysis. Geomorphology 134 (1-2), 157–170.

Garfunkel, Z., Ben-Avraham, Z., 1996. The structure of the Dead Sea basin. Tectonophysics 266, 155–176.

Gavrieli, I., Oren, A., 2004. The Dead Sea as a Dying Lake. In: Nihoul, J. C. J., Zavialov, P. O., Micklin, P. P. (Eds.), Dying Dead Seas Clim. Versus Anthr. Causes SE - 11. Vol. 36 of NATO Science Series IV: Earth and Environmental Sciences. Springer Netherlands, pp. 287–305.

Goldscheider, N., Drew, D., 2007. Methods in Karst Hydrogeology. Taylor and Francis, London, UK.

Gutiérrez, F., Fabregat, I., Roqué, C., Carbonel, D., Guerrero, J., García-Hermoso, F., Zarroca, M., Linares, R., 2016. Sinkholes and caves related to evaporite dissolution

in a stratigraphically and structurally complex setting, Fluvia Valley, eastern Spanish Pyrenees. Geological, geomorphological and environmental implications. Geomorphology 267, 76–97.

Gutiérrez, F., Guerrero, J., Lucha, P., 2008. A genetic classification of sinkholes illustrated from evaporite paleokarst exposures in Spain. Environ. Geol. 53 (5), 993–1006.

Gutiérrez, F., Lizaga, I., 2016. Sinkholes, collapse structures and large landslides in an active salt dome submerged by a reservoir: The unique case of the Ambal ridge in the Karun River, Zagros Mountains, Iran. Geomorphology 254, 88–103.

Gutierréz, F., Parise, M., De Waele, J., Jourde, H., 2014. A review on natural and human-induced geohazards and impacts in karst. Earth-Science Rev. 138, 61–88.

Harwin, S., Lucieer, A., 2012. Assessing the accuracy of georeferenced point clouds produced via multi-view stereopsis from Unmanned Aerial Vehicle (UAV) imagery. Remote Sens. 4, 1573–1599.

Hatzor, Y. H., Wainshtein, I., Bakun Mazor, D., 2010. Stability of shallow karstic caverns in blocky rock masses. Int. J. Rock Mech. Min. Sci. 47 (8), 1289–1303.

Holohan, E. P., Schöpfer, M. P. J., Walsh, J. J., 2011. Mechanical and geometric controls on the structural evolution of pit crater and caldera subsidence. J. Geophys. Res. 116 (B07202).

Intrieri, E., Gigli, G., Nocentini, M., Lombardi, L., Mugnai, F., Fidolini, F., Casagli, N., 2015. Sinkhole monitoring and early warning: An experimental and successful GB-InSAR application. Geomorphology 241, 304–314.

Kaufmann, G., 2014. Geophysical mapping of solution and collapse sinkholes. J. Appl. Geophys. 111, 271–288.

Kaufmann, G., Braun, J., 2000. Karst Aquifer evolution in fractured, porous rocks. Water Resour. Res. 36 (6), 1381–1391.

Kaufmann, G., Romanov, D., Nielbock, R., 2011. Cave detection using multiple geophysical methods: Unicorn cave, Harz Mountains, Germany. Geophysics 76 (3), B71–B77.

Kawashima, K., Aydan, Ö., Aoki, T., Kishimoto, I., Konagai, K., Matsui, T., Sakuta, J., Takahashi, N., Teodori, S.-P., Yashima, A., 2010. Reconnaissance Investigation on the Damage of the 2009 L'Aquila, Central Italy Earthquake. J. Earthq. Eng. 14 (6), 817–841.

Khlaifat, A., Al-Khashman, O., Qutob, H., 2010. Physical and chemical characterization of Dead Sea mud. Mater. Charact. 61 (5), 564–568.

Khoury, H. N., 2002. Clays and clay minerals in Jordan. Tech. rep., Jordan University, Amman, Jordan.

Kohl, M., 2001. Subsidence and sinkholes in East Tennessee. Tech. rep., State of Tennessee, Department of Environment and Conservation, Division of Geology, Tennessee.

Kottmeier, C., Agnon, A., Al-Halbouni, D., Alpert, P., Corsmeier, U., Dahm, T., Eshel, A., Geyer, S., Haas, M., Holohan, E. P., Kalthoff, N., Kishcha, P., Krawczyk, C. M., Lati, J., Laronne, J. B., Lott, F., Mallast, U., Merz, R., Metzger, J., Mohsen, A., Morin, E., Nied, M., Rödiger, T., Salameh, E., Sawarieh, A., Shannak, B., Siebert, C., Weber, M., 2016. New perspectives on interdisciplinary earth science at the Dead Sea : the DESERVE project. Sci. Total Environ. 544, 1045–1058.

Kotyrba, A., 2015. A study of sinkhole hazard at area of Locked Colliery. In: Post-Mining. Nancy.

Krawczyk, C., Dahm, T., 2011. Charakterisierung und Überwachung von Salz-bezogenen Erdfällen in urbanen Gebieten. Tech. rep., Leibnitz Institute of Applied Geophysics, Hannover, Germany.

Krawczyk, C. M., Polom, U., Alrshdan, H., Al-Halbouni, D., Sawarieh, A., Dahm, T., 2015. New process model for the Dead Sea sinkholes at Ghor Al Haditha, Jordan, derived from shear-wave reflection seismics. In: EGU Gen. Assem. 2015. Vienna, Austria.

Le Béon, M., Klinger, Y., Mériaux, A. S., Al-Qaryouti, M., Finkel, R. C., Mayyas, O., Tapponnier, P., 2012. Quaternary morphotectonic mapping of the Wadi Araba and implications for the tectonic activity of the southern Dead Sea fault. Tectonics 31 (5), 1–25.

Legchenko, A., Ezersky, M. G., Boucher, M., Camerlynck, C., Al-Zoubi, A., Chalikakis, K., 2008. Pre-existing caverns in salt formations could be the major cause of sinkhole hazards along the coast of the Dead Sea. Geophys. Res. Lett. 35 (19), 1–5.

Lensky, N. G., Dvorkin, Y., Lyakhovsky, V., Gertman, I., Gavrieli, I., 2005. Water, salt, and energy balances of the Dead Sea. Water Resour. Res. 41 (12), 1–13.

Leon, J., Roelfsema, C. M., Saunders, M. I., Phinn, S. R., 2015. Measuring coral reef terrain roughness us-

ing "Structure-from-Motion" close-range photogramme-
try. Geomorphology 242, 21–28.

Lollino, P., Martimucci, V., Parise, M., 2013. Geological sur-
vey and numerical modeling of the potential failure mech-
anisms of underground caves. Geosystem Eng. 16 (1), 37–
41.

Luhmann, T., Robson, S., Kyle, S., Boehm, J., 2014. Close-
range photogrammetry and 3D imaging, 2nd Edition.
Walter De Gruyter.

Mallast, U., Gloaguen, R., Geyer, S., Rödiger, T., Siebert,
C., 2011. Derivation of groundwater flow-paths based
on semi-automatic extraction of lineaments from remote
sensing data. Hydrol. Earth Syst. Sci. 15 (8), 2665–2678.

Margiotta, S., Negri, S., Parise, M., Valloni, R., 2012. Map-
ping the susceptibility to sinkholes in coastal areas, based
on stratigraphy, geomorphology and geophysics. Nat. Haz-
ards 62 (2), 657–676.

Menzel, L., Teichert, E., Weiss, M., 2007. Climate change
impact on the water resources of the semi-arid Jordan
region. In: Proc. 3rd Int. Conf. Clim. Water, Helsinki.
pp. 320–325.

Messerklinger, S., 2014. Formation mechanism of large subsi-
dence sinkholes in the Lar valley in Iran. Q. J. Eng. Geol.
Hydrogeol. 47, 237–250.

MWI, 2013. Jordan Water Sector Facts and Figures. Tech.
rep., Ministry of Water and Irrigation, Amman, Jordan.

Nof, R. N., Baer, G., Ziv, A., Raz, E., Atzori, S., Salvi,
S., 2013. Sinkhole precursors along the Dead Sea, Israel,
revealed by SAR interferometry. Geology 41 (9), 1019–
1022.

Odeh, T., Rödiger, T., Geyer, S., Schirmer, M., 2015. Hydro-
logical modelling of a heterogeneous catchment using an
integrated approach of remote sensing, a geographic in-
formation system and hydrologic response units: the case
study of Wadi Zerka Ma'in catchment area, north east of
the Dead Sea. Environ. Earth Sci. 73 (7), 3309–3326.

Oz, I., Eyal, S., Yoseph, Y., Ittai, G., Elad, L., Haim, G.,
2016. Salt dissolution and sinkhole formation: Results of
laboratory experiments. J. Geophys. Res. Earth Surf., 1–
17.

Panno, S. V., Kelly, W. R., Angel, J. C., Luman, D. E., 2013.
Hydrogeologic and topographic controls on evolution of
karst features in Illinois' sinkhole plain. Carbonates and
Evaporites 28 (1-2), 13–21.

Parise, M., 2008. Rock failures in karst. In: Proc. 10th Int.
Symp. landslides, Xi'an. Vol. 1. pp. 275–280.

Parise, M., 2010. Hazards in karst. In: Sustain. Karst Envi-
ron. Dinaric Karst Other Karst Reg. Series on Groundwa-
ter, IHP-UNESCO, Plitvice Lakes, Croatia, pp. 155–162.

Parise, M., 2015. A procedure for evaluating the susceptibil-
ity to natural and anthropogenic sinkholes. Georisk As-
sess. Manag. Risk Eng. Syst. Geohazards 9 (4), 272–285.

Parise, M., Lollino, P., 2011. A preliminary analysis of failure
mechanisms in karst and man-made underground caves in
Southern Italy. Geomorphology 134 (1-2), 132–143.

Parise, M., Perrone, A., Violante, C., Stewart, J. P., Si-
monelli, A., Guzzetti, F., 2010. Activity of the Italian
National Research Council in the aftermath of the 6 April
2009 Abruzzo earthquake: the Sinizzo Lake case study. In:
Proc. 2nd Int. Work. Catastrophic Sink. Nat. Anthropog.
Environ. Rome. pp. 623–641.

Polom, U., Alrshdan, H., Al-Halbouni, D., Sawarieh, A.,
Dahm, T., Krawczyk, C., 2016. Improved Dead Sea sink-
hole site characterization at Ghor Al Haditha, Jordan,
based on repeated shear wave reflection seismic profiling.
In: EGU Gen. Assem. 2016. Vienna, Austria.

Reddish, D. J., Whittaker, B. N., 2012. Subsidence: occur-
rence, prediction and control. Vol. 56. Elsevier.

Salameh, E., 2016. Effects of Climatic Changes on Surface
and Groundwater Resources in the Northwestern Part of
Jordan. Int. J. Environ. Agric. Res. 2 (1).

Salameh, E., El-Naser, H., 2000. Changes in the Dead Sea
Level and their Impacts on the Surrounding Groundwater
Bodies. Acta Hydrochim. Hydrobiol. 28 (1), 24–33.

Salameh, E., Hammouri, R., 2008. Sources of groundwater
salinity along the flow path, Disi - Dead Sea/Jordan. En-
viron. Geol. 55, 1039–1053.

Sawarieh, A., Al Adas, A., Al Bashish, A., Al Seba'i, E.,
2000. Sinkholes Phenomena At Ghor Al Haditha Area -
Internal Report No. 12. Tech. rep., Natural Resources Au-
thority, Amman, Jordan.

Shalev, E., Lyakhovsky, V., 2012. Viscoelastic damage mod-
eling of sinkhole formation. J. Struct. Geol. 42, 163–170.

Shalev, E., Lyakhovsky, V., Yechieli, Y., 2006. Salt dissolu-
tion and sinkhole formation along the Dead Sea shore. J.
Geophys. Res. 111 (B3102).

Siebert, C., Mallast, U., Rödiger, T., Ionescu, D., Schwonke, F., Hall, J., Sade, A., Pohl, T., Merkel, B., 2014a. Multiple sensor tracking of submarine groundwater discharge: concept study along the Dead Sea. In: EGU Gen. Assem. Vol. 16. European Geoscience Union, Vienna, Austria, p. 11217.

Siebert, C., Rödiger, T., Mallast, U., Gräbe, A., Guttman, J., Laronne, J. B., Storz-Peretz, Y., Greenman, A., Salameh, E., Al-Raggad, M., Vachtman, D., Zvi, A. B., Ionescu, D., Brenner, A., Merz, R., Geyer, S., 2014b. Challenges to estimate surface- and groundwater flow in arid regions: The Dead Sea catchment. Sci. Total Environ. 485-486, 828–841.

Siebert, C., Mallast, U., Rödiger, T., Strey, M., Ionescu, D., Häusler, S., Noriega, B., 2014c. Submarine groundwater discharge at the Dead Sea. 23rd Water Intrusion Meet. Husum, Ger., 366–370.

Smit, J., Brun, J.-P., Fort, X., Cloetingh, S., Ben-Avraham, Z., 2008. Salt tectonics in pull-apart basins with application to the Dead Sea Basin. Tectonophysics 449, 1–16.

Stein, M., Torfstein, A., Gavrieli, I., Yechieli, Y., 2010. Abrupt aridities and salt deposition in the post-glacial Dead Sea and their North Atlantic connection. Quat. Sci. Rev. 29, 567–575.

Taqieddin, S. a., Abderahman, N. S., Atallah, M., 2000. Sinkhole hazards along the eastern Dead Sea shoreline area, Jordan: a geological and geotechnical consideration. Environ. Geol. 39 (11), 1237–1253.

Ten Brink, U., Ben-Avraham, Z., 1989. The anatomy of a pull-apart basin; seismic reflection observations of the Dead Sea basin. Tectonics 8 (2), 333–350.

Tessari, G., Floris, M., 2014. Characterization and Modelling of geological instabilities through remote sensing techniques and numerical simulations. Tech. rep., Università degli Studi di Padova, Padua, Italy.

Tharp, T., 2002. Poroelastic analysis of cover-collapse sinkhole formation by piezometric surface drawdown. Environ. Geol. 42 (5), 447–456.

Tharp, T. M., 1999. Mechanics of upward propagation of cover-collapse sinkholes. Eng. Geol. 52 (1-2), 23–33.

USGS, 2015. Corona declassified satellite imagery, url=https://lta.cr.usgs.gov/declass_1, date accessed 2015-08-13.

Walter, T., 2014. Cost effective aero-photogrammetry toys at active volcanoes: On the use of drones, balloons and kites. In: EGU Gen. Assem. Conf. Abstr. Vol. 16. European Geoscience Union, Vienna, Austria, p. 6427.

Waltham, A., Fookes, P., 2005. Engineering classification of karst ground conditions. Q. J. Eng. Geol. Hydrogeol. 3 (1), 1–20.

Waltham, T., 2016. Control the drainage: the gospel accorded to sinkholes. Q. J. Eng. Geol. Hydrogeol. 49 (1), 5–20.

Waltham, T., Bell, F., Culshaw, M. G., 2005. Sinkholes and subsidence: Karst and Cavernous Rocks in Engineering and Construction. Springer, Berlin, Heidelberg.

Whitman, D., Gubbels, T., Powell, L., 1999. Spatial Interrelationships between Lake Elevations, Water Tables, and Sinkhole Occurrence in Central Florida: A GIS Approach. Photogramm. Eng. Remote Sensing 65 (10), 1169–1178.

World Bank, 2016. Population growth indicator, url=https://data.worldbank.org/indicator/sp.pop.grow, date accessed 2016-01-14.

Yechieli, Y., Abelson, M., Baer, G., 2015. Sinkhole formation and subsidence along the Dead Sea coast, Israel. Hydrogeol. J.

7. Acknowledgements

Appendix A.

A.1. Bundle adjustment algorithm

We summarize here the mathematical fundamentals of the bundle adjustment algorithm used for multi-image triangulation in close-range photogrammetry based on detailed descriptions in Förstner and Wrobel (2013) and Luhmann et al. (2014).

A.1.1. Collinearity equations

Looking at one single image first, the interior coordinate system (image frame, (x', y', z')) of the camera is known, including the offset z' of its perspective center ($\boldsymbol{X_0}$) in relation to the origin of the reference exterior coordinate frame (global or object coordinate system, (X,Y,Z)).

The angular orientation ($\boldsymbol{\Phi} = \omega, \varphi, \kappa$) in space of the image coordinate system is defined by a rotation matrix $\boldsymbol{R}$ about the global coordinate system:

$$\boldsymbol{R} = \begin{pmatrix} r_{11} & r_{12} & r_{13} \\ r_{21} & r_{22} & r_{23} \\ r_{31} & r_{32} & r_{33} \end{pmatrix} \qquad \text{(A.1)}$$

Using a Helmert coordinate system transformation any point of the image ($\boldsymbol{x'}$) can now be translated from camera coordinates into the global coordinates, denoting the vector from the perspective center to the image point within the object coordinate system with $\boldsymbol{X^*}$, so that $\boldsymbol{X} = \boldsymbol{X_0} + \boldsymbol{X^*}$. The image vector can be expressed by scaling (m) and rotation as $\boldsymbol{X^*} = m\boldsymbol{R} \cdot \boldsymbol{x'}$. The projection of an image point into the object point is therefore:

$$\boldsymbol{X} = \boldsymbol{X_0} + m\boldsymbol{R} \cdot \boldsymbol{x'} = \boldsymbol{X_0} + \boldsymbol{X^*} \qquad \text{(A.2)}$$

For a 3D inversion of this problem for one image point more information is needed in the form of intersection with additional image ray paths or surfaces. With $\boldsymbol{x'_0}$ as a principal point in the camera coordinate system and $\boldsymbol{\Delta x'}$ as internal image distortion parameters, the inversion equation reads as:

$$\boldsymbol{x'} - \boldsymbol{x'_0} - \boldsymbol{\Delta x'} = \frac{1}{m}\boldsymbol{R^{-1}} \cdot (\boldsymbol{X} + \boldsymbol{X_0}) \qquad \text{(A.3)}$$

The scaling factor is eliminated by internal division of the first two rows by the third in Eq. A.3. This leads to the general collinearity equations for transformation of object (exterior) coordinates into image (interior) coordinates as function of the orientation parameters stated above, expressed here in vector entries notation:

$$
\begin{aligned}
x' = x'_0 + \Delta x' + \\
z' \frac{r_{11}(X - X_0) + r_{21}(Y - Y_0) + r_{31}(Z - Z_0)}{r_{13}(X - X_0) + r_{23}(Y - Y_0) + r_{33}(Z - Z_0)} \\
y' = y'_0 + \Delta y' + \\
z' \frac{r_{12}(X - X_0) + r_{22}(Y - Y_0) + r_{32}(Z - Z_0)}{r_{13}(X - X_0) + r_{23}(Y - Y_0) + r_{33}(Z - Z_0)}
\end{aligned}
$$
$$\text{(A.4)}$$

A.1.2. Space resection

In the case of a fixed interior coordinate system of e.g. a metric digital camera, at minimum three reference points in the object frame providing the position and orientation parameters are needed for the non-linear solution of the collinearity equations (A.4) with approximate starting values. A unique solution will be achieved with four reference points and each 3D reference point provides three correction equations. A Taylor-series expansion linearisa-

tion and a least-squares fit is used for solving the resulting normal correction equations. For multi-image processing it has the general form:

$$\boldsymbol{X}_i' + v\boldsymbol{X}_i' = F(\boldsymbol{X}_i, \boldsymbol{X}_{0j}, \boldsymbol{\Delta x}_k', \boldsymbol{x}_{0k}', \boldsymbol{\Phi}_j) \quad \text{(A.5)}$$

with indices: i: image point, j: image and k: camera

The number of unknowns (u) in this set of equations can be calculated using reference points via:

$$u = u_I\, n_{\text{images}} + u_P\, n_{\text{points}} + u_C\, n_{\text{cameras}} \quad \text{(A.6)}$$

with u_I = six parameters of exterior orientation, u_P = three parameters for the position of each point and u_C = zero to more than three parameters of the interior orientation per camera. Additional constraints, e.g. measured distances or object surfaces can be included in the correction equations leading to less degrees of freedom. In the case of a non-fixed interior coordinate system at minimum five reference points are needed to apply a Direct Linear Transformation method that does not need approximate initial values. For further reading and the mathematical details of these procedures refer to Luhmann et al. (2014).

A.2. Additional field and aerial photo evidence

We present the main equipment used in this study, namely the Helikite balloon used for acquisition of the aerial images (Fig. A.1A) and the differential GPS device used for ground referencing (Fig. A.1B). Finally, we provide an assemblage of further field and aerial photo evidence of the structures, sinkholes and streams/springs in the measurement area referred to in the main text (Section
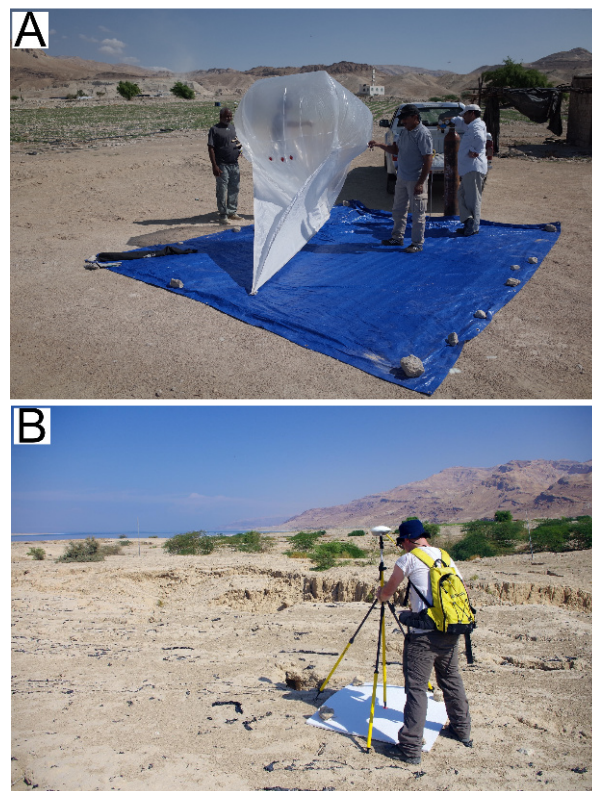
Fig. A.1: Field equipment used for the photogrammetric survey. **A**: Filling and reeling out the camera bearing Helikite balloon. **B**: Measuring the ground control points with a high accuracy Differential GPS.

4). A ground-based view of the non-tectonic faults bounding the main depression area is given in Fig. A.2A. The detailed aerial photos highlight a sinkhole cluster sequence (B), individual salt accumulations (C) and the range of water infilling of the sinkholes (D).
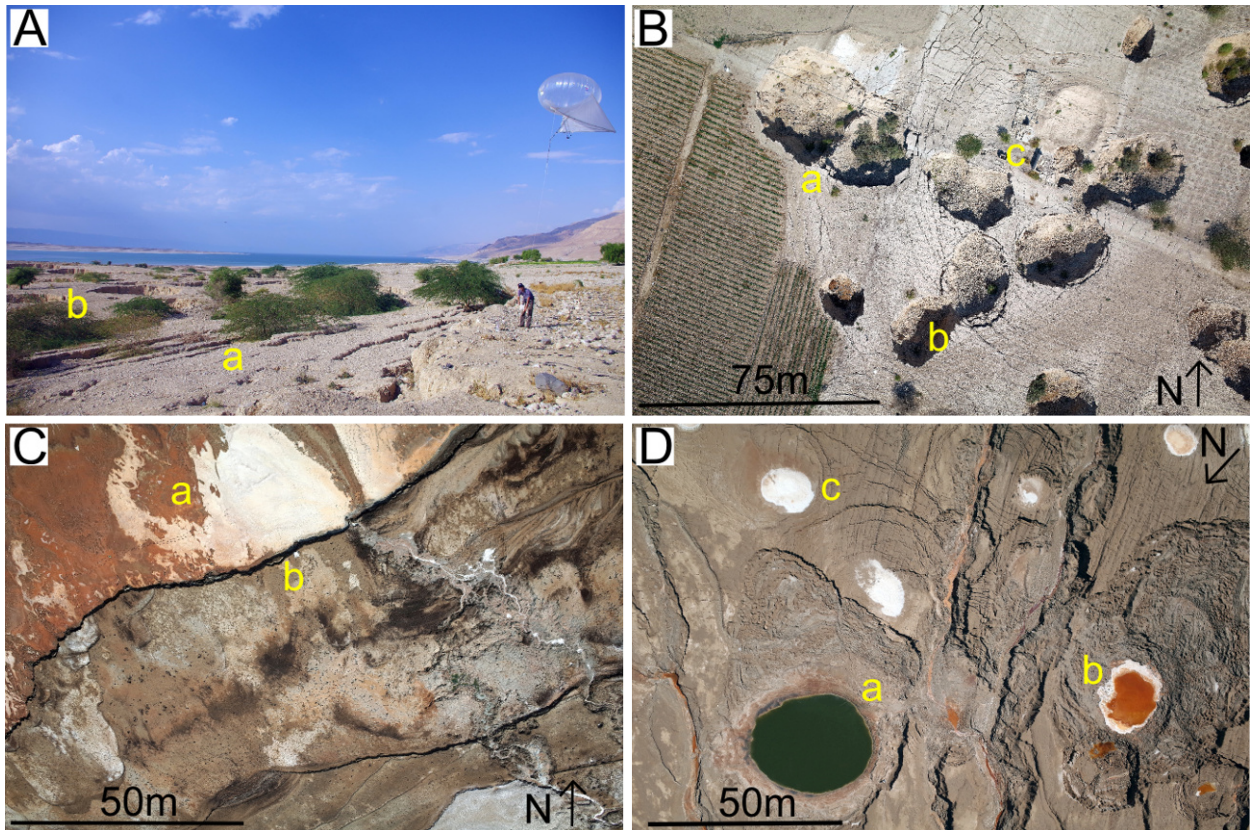
Fig. A.2: Geomorphological structures in alluvium and mud. **A**: Major cracks (**a**) bounding the main depression zone at the fractured edge of the sinkhole area in the alluvium (**b**). **B**: Sinkhole cluster in the alluvium. Indicated are nested sinkholes (**a,b**) and a destroyed farm building (**c**). **C**: The retreat of the shoreline and the existence of individual salt pans (**a**), built by evaporation of closed salt-water ponds. Marker point a the edge of an old shoreline (**b**). **D**: Heterogeneous water filling of mud-flat sinkholes: Fresh-water (**a**), salt-water with high iron-oxide content (**b**) and dried out former salt-water sinkhole (**c**). Several older sinkholes of the nest zone are nowadays dry (**b**).